

CHEMICAL COMPOSITIONS OF THIN-DISK, HIGH-METALLICITY RED HORIZONTAL-BRANCH FIELD STARS

M. Afşar^{1,2}, C. Sneden², and B.-Q. For^{2,3}

ABSTRACT

We present a detailed abundance analysis and atmospheric parameters of 76 stars from a survey to identify field Galactic red horizontal-branch (RHB) stars. High-resolution echelle spectra ($R \simeq 60,000$, $S/N \geq 100$) were obtained with 2.7 m Smith Telescope at McDonald Observatory. The target stars were selected only by color and parallax information. Overall metallicities and relative abundances of proton-capture elements (C I, N I, O I, Li I), α -elements (Ca I and Si I), and neutron-capture elements (Eu II and La II) were determined by either equivalent width or synthetic spectrum analyses. We used CN features at $\lambda\lambda 7995\text{--}8040$ region in order to determine $^{12}\text{C}/^{13}\text{C}$ ratios of our targets. Investigation of the evolutionary stages, using spectroscopic T_{eff} and $\log g$ values along with derived $^{12}\text{C}/^{13}\text{C}$ ratios, revealed the presence of 18 probable RHB stars in our sample. We also derived kinematics of the stars with available distance information. Taking into account both the kinematics and probable evolutionary stages, we conclude that our sample contains five thick disk and 13 thin disk RHB stars. Up until now, RHB stars have been considered as members of the thick disk, and were expected to have large space velocities and sub-solar metallicities. However, our sample is dominated by low velocity solar-metallicity RHB stars; their existence cannot be easily explained with standard stellar evolution.

Subject headings: Galaxy: evolution — stars: abundances — stars: evolution — stars: kinematics

¹Department of Astronomy and Space Sciences, Ege University, 35100 Bornova, İzmir, Turkey; me-like.afsar@ege.edu.tr

²Department of Astronomy and McDonald Observatory, The University of Texas, Austin, TX 78712; afsar,chris,biqing@astro.as.utexas.edu

³ICRAR, University of Western Australia, 35 Stirling Hwy, Crawley, WA 6009, Australia; biqing.for@uwa.edu.au

1. INTRODUCTION

In conjunction with onset of quiescent helium fusion, stars locate on the zero-age horizontal branch (HB) of the HR diagram. Usually HB stars have two energy sources: in addition to the helium burning in their cores, they experience hydrogen fusion in a surrounding shell. The HB domain encompasses a very large effective temperature range, leading to stars being labeled as members of the extreme HB, blue HB, RR Lyrae variables, red HB (RHB), and red clump (RC) stars. The loci of the stars on HB partly depends on many parameters, including stellar mass, metallicity, age, helium abundance, and rotation, and mass. Mass is a key parameter: HB locations depend sensitively on initial stellar masses or the amount of mass loss encountered during the red giant branch (RGB) phase. Theoretical models (e.g. Sweigart & Gross 1978, Piersanti et al. 2004) suggest that very low mass stars (around $0.5 M_{\odot}$) appear on the blue part of the HB, higher-mass ones (around $0.8 M_{\odot}$) sit on the RHB, and stars of solar mass and greater are located in the small RC area at the extreme red edge of the HB.

RHBs are located between the instability strip and the RC. Stars of the RC concentrate at $M_V \approx 1$ and $B-V \approx 0.9-1$ (Cannon 1970, Wilson 1976). These colors correspond to effective temperatures $T_{\text{eff}} \approx 5000-4800$ K (e.g. Ramírez & Meléndez 2005), in contrast to the color/ T_{eff} range of RHB stars $(B-V)_0 \approx 0.5-0.8$, $T_{\text{eff}} \approx 5000-6200$ K (Straizys et al. 1981, Gray & Corbally 2009). It is easy to identify RHB stars in globular cluster (GC) color-magnitude diagrams (e.g, see the survey of Rosenberg et al. 2000a, Rosenberg et al. 2000b) but they are not easily distinguished from RC, SGB (subgiant branch), and even MS (main sequence) stars in the Galactic field. There have been several attempts to isolate field RHB stars. An early systematic survey was that of Straizys et al. (1981), who observed eight RHB candidates with the Vilnius photometric system. They derived the metallicities and determined the luminosity classes using color-color diagrams, but could not prove their RHB membership because of lack of surface gravity information.

Field RHB stars were first investigated as a group by Rose (1985). He studied G5-G7 stars selected from the Uggren (1962, 1963) North Galactic Pole (NGP) survey. By analyzing low resolution spectroscopic data, Rose showed that one can distinguish between evolved and “post-main sequence stars” (i.e, subgiants) using the strengths of Sr II $\lambda 4077$ Å and CN $\lambda 3883$ and 4216 Å bands. He also estimated the scale height of RHBs to be > 500 pc and concluded that they are moderately metal-poor members of the “thick disk” (Gilmore & Reid 1983) of the Galaxy.

The RHB assignments subsequently were questioned by Norris (1987), who reported the results of photometric observations of ten Uggren (1962, 1963) stars that formed part of the Rose (1985) RHB candidate sample. Norris argued that the colors of these stars

(e.g., $B - V \approx 0.88$) are indistinguishable from the RC stars in the old disk, mildly metal-deficient open cluster NGC 2243 ($t \approx 4$ Gyr, Anthony-Twarog et al. 2005; $[\text{Fe}/\text{H}] \approx -0.4$, Jacobson et al. 2011). In fact, the colors of the Rose candidates have almost no overlap with the colors of true RHB stars ($0.6 \lesssim B - V \lesssim 0.8$; e.g., Hesser et al. 1987) of the globular cluster 47 Tuc ($t \approx 13$ Gyr, Anthony-Twarog et al. (2005); $[\text{Fe}/\text{H}] = \approx -0.7$, Hesser et al. (1987)).

The evolutionary states of alleged RHB field stars were revisited by Tautvaišienė (1996), who carried out Vilnius system photometric observations of 13 field RHB candidates from Rose (1985). From these data she deduced spectral types, atmospheric parameters and absolute magnitudes. Her results yielded a complex message: low mean metallicity ($\langle [\text{Fe}/\text{H}] \rangle \approx -0.6$) and large mean age ($t \approx 10\text{--}12$ Gyr) consistent with possible RHB status, but low mean temperature ($\langle T_{\text{eff}} \rangle \approx 4940$ K) consistent with the RC.

In another study, Tautvaišienė (1997) gathered high-dispersion spectra of 10 field RHB stars that had been identified in a number of previous papers. The metallicity range of her sample was very large, $-0.2 \geq [\text{Fe}/\text{H}] \geq -1.9$, which resulted in mixed Galactic population membership. She concluded that the chemical compositions of these RHB stars were in accord with those of dwarf and red giant stars of similar metallicities, and thus RHB stars can be used as tracers of the chemical evolution of the Galaxy. Tautvaišienė et al. (2001) followed this paper with another chemical composition study of Rose (1985) stars, finding in particular: (a) overabundances of α -elements (O, Mg, Si, Ca, Ti); (b) solar abundances of some neutron-capture elements (Y, Ba, La) and overabundances of others (especially Eu, possibly Zr and Sm); (c) depleted C and enriched N abundances, indicative of CN-cycle H-fusion in these stars; and (d) perhaps most importantly, very low carbon isotope ratios, $^{12}\text{C}/^{13}\text{C} \approx 3\text{--}6$.

Previous studies have suggested that true field RHB stars are relatively rare, but the extant sample sizes are small. The ones that exist should be relatively low mass members of the thick disk because stellar evolution models (e.g. Lee et al. 1994) predict that higher-mass, solar-metallicity core He-burning stars should reside exclusively in the RC. Following the Norris (1987) suggestion that, “the only way to resolve this problem in an unambiguous way will be to analyze a complete sample of stars having colors in the range $0.7 \leq B - V \leq 0.95$ ”, Kaempf et al. (2005) identified a large sample of RHB candidates from the Hipparcos catalog (Perryman et al. 1997). Their kinematic analysis found both thick disk and halo RHBs, and they estimated a Galactic scale height of 0.6 kpc for the thick disk RHBs.

In this paper we report on a new large-sample chemical composition study of candidate field RHB stars. The combined kinematics, metallicities, and chemical abundance ratios will be used to confirm the existence of a substantial number of high-metallicity thin-disk

RHB stars. In §2 we present the target star selection and the spectroscopic data that were gathered. Model atmosphere parameter derivation is described in §3. We discuss the chemical composition analysis in §4, along with comparison to other large-sample literature studies. The kinematics of our sample are given in §5, and estimates of their evolutionary states in §6. We discuss the implications of these results in §7.

2. OBSERVATIONS

We obtained high resolution, high signal-to-noise spectra of stars selected mainly by their colors (as suggested above) and some indications that they might be giants (spectral luminosity class III and/or low M_V from Hipparcos parallax).

2.1. Selection of the Program Stars

We assembled our program star list from several sources. Most of our RHB candidates were selected from among the Upgren (1962) NGP survey and the Harlan (1969, 1974, 1981) stars used by Rose (1985). We also made use of SIMBAD¹ and VizieR².

We restricted the prospective sample in color, spectral type, and apparent magnitude ($V < 11$). For spectral type, we limited our search to between G0III and G8III. The reason for this restriction is simple: the loci of the RHB stars in the HR diagram fall in between the instability strip on the blue side and RC region on the red side. RHB stars have very similar luminosities to RC stars, although the effective temperatures of RCs are lower. For RC stars Kaempf et al. (2005) adopted a luminosity-dependent color range of $0.85 \lesssim B-V \lesssim 1.2$ (spectral classes approximately G6–K3), and for RHB stars $0.5 \lesssim B-V \lesssim 0.8$ (approximately G0–G5); see their Figure 1. In our color selection we used this RHB $B-V$ range, but when possible we preferred to use an equivalent $V-K$ range of ≈ 1.5 – 2.2 , because $V-K$ colors are almost independent of metallicity and gravity but very sensitive to effective temperature. In order to calculate photometric temperatures we have used the metallicity-dependent T_{eff} -color formula for giants given by Ramírez & Meléndez (2005). The apparent magnitude limit was defined by our telescope/instrument combination; see §2.2. The radial velocity and proper motion properties of the candidates were not included in the selection criteria, which allowed us to minimize potential kinematic biases in our sample. There is an inevitable

¹<http://simbad.u-strasbg.fr/simbad/>

²<http://vizier.u-strasbg.fr/viz-bin/VizieR>

bias due to the cutoff in apparent magnitude limit of the instrumental set-up.

2.2. Observations and data reduction

We obtained high-resolution spectra of RHB candidates with the Robert G. Tull Cross-Dispersed Echelle spectrograph (Tull et al. 1995) of the 2.7m Harlan J. Smith Telescope at McDonald Observatory. The instrumental setup, including a $1''.2$ width entrance slit, yielded a spectral resolving power of $R \equiv \lambda/\Delta\lambda \approx 60000$. Within the wavelength coverage of $\lambda\lambda$ 3400-10900, we observed 63 spectral orders. The gaps between the orders reduce towards blue orders, enabling continuous spectral coverage for $\lambda \lesssim 5900$ Å. The data were obtained during five observing runs corresponding to 22 nights in total.

Based on the selection criteria discussed in §2.1, we were able to observe 129 candidate RHB stars with adequate signal-to-noise. Not all of the stars survived scrutiny after data reduction. Some of these stars were of interest because they were being observed with high spectral resolution for the first time. Inspection of the data revealed that 20 candidates either were rapidly rotating ($V \sin i \geq 30$) or were double-lined spectroscopic binaries. These were discarded from the final sample because in both cases the spectral features become too blended and do not allow us to extract meaningful abundances for this project. In the end we also had to eliminate 33 more candidates during the model atmosphere analyses because we were not be able to obtain reasonable atmospheric parameters from spectroscopic criteria alone (see §3 for further discussion). The remaining sample of 76 candidates were studied in detail. In Table 1 we present basic data for these program stars.

The data reductions were performed with the IRAF³ software package in the classical manner: bias subtraction, flat-field division, and scattered light removal followed by extraction of the spectral orders. We took at least two exposures per star and combined them in order to filter out cosmic rays events. Fast-rotating hot stars were observed each night at appropriate air-masses, and used to remove telluric features from the spectra of the program stars. Removal of the telluric lines was done with the IRAF routine *telluric*, following continuum normalization. ThAr lamp exposures taken at the beginning and end of each night were used for the wavelength calibration, again done with standard IRAF tasks.

Since some of the RHB candidates have reported parallaxes but no radial velocities

³The Image Reduction and Analysis Facility, a general purpose software package for astronomical data, is written and supported by the IRAF programming group of the National Optical Astronomy Observatory (NOAO) in Tucson, AZ, USA.

(RVs), we also observed a few IAU RV standards. We used these standards to measure the RVs of our stars via the cross-correlating technique provided in *fxcor* (Fitzpatrick 1993) task in IRAF. The mean RVs of the relevant stars are listed in Table 1. Typical errors for the RV measurements were around ± 0.3 - 0.6 km s $^{-1}$. We also checked our measurements by re-measuring the RVs of a few of our program stars that have previously published values. Our RVs agree with the literature values to within the joint error estimates.

We estimated signal-to-noise (S/N) ratios of the spectra at three different “continuum” wavelength regions near 4500, 5500 and 6500 Å in which we detect no obvious absorption features. We give examples of the derived S/N for three program stars with different visual magnitudes in Table 2.

3. MODEL ATMOSPHERE PARAMETERS

We have used both equivalent widths (EW s) and spectrum synthesis for the abundance analysis. The line list for model atmospheric parameter determination was generated by choosing clean lines with laboratory gf -values between $\lambda 5500$ - 6500 Å. This spectral region contains many relatively unblended Fe-peak species transitions and only very weak CN molecular contamination in our program stars. In selecting the transitions we consulted the solar line compendium of Moore et al. (1966) and the Griffin (1968) Arcturus spectral atlas. We measured EW s using the SPECTRE⁴ code (Fitzpatrick & Sneden 1987). SPECTRE employs a semi-automated routine that fits Voigt and Gaussian line profiles to the observed spectral lines.

In Figure 1 we compare our EW measurements with the values given by Takeda et al. (2005) for HIP 13339 and HIP 71837. The EW scales are in reasonable agreement: defining $\Delta EW \equiv EW_{literature} - EW_{thisstudy}$, we found $\langle \Delta EW \rangle = +1.6$ mÅ, with $\sigma \simeq 5$ mÅ.

Stellar atmosphere models required by the analysis were from the Castelli et al. (1997), Castelli & Kurucz (2003) grid⁵ of model atmospheres computed with opacity distribution functions and without convective overshooting. We interpolated in this grid with software developed by Andy McWilliam and Inese Ivans. Then we used an automated version of the spectral line analysis and synthetic spectrum code MOOG (Sneden 1973)⁶ to determine the abundances of our program stars. MOOG performs analyses using one-dimensional

⁴ An interactive spectrum measurement package, available at <http://www.as.utexas.edu/~chris/spectre.html>

⁵ Available at: <http://kurucz.harvard.edu/grids.html>

⁶ available at <http://www.as.utexas.edu/~chris/moog.html>

local thermodynamic equilibrium (LTE) equations for plane parallel atmospheres. In the automated version (described in more detail by Hollek et al. 2011 and Roederer et al., in preparation) all of the steps in model atmosphere derivation and many parts in the relative abundance analysis are done iteratively by the code without human intervention.

We used Fe I and Fe II abundances derived with trial model stellar atmospheres to determine the fundamental stellar parameters of effective temperature T_{eff} , surface gravity, $\log g$, microturbulent velocity ξ_t , and metallicity $[\text{Fe}/\text{H}]$ ⁷. Final values of T_{eff} were estimated by requiring that Fe I abundances show no trend with excitation potential χ beyond internal line-to-line scatter uncertainties. A similar approach yielded estimates of ξ_t , which is related to small-scale turbulent motion: this parameter was varied until we obtained no apparent Fe I abundance trend with reduced width RW ($\equiv EW/\lambda$).

As reported in previous studies, non-local thermodynamical equilibrium (NLTE) mechanism almost has no effect on Fe II lines and has a small effect on Fe I lines for solar-type metallicities and mildly metal-poor stars. As given by Mashonkina et al. (2011) for a temperature range of 4600–6500 K, the departure from LTE is not more than 0.1 dex in Fe I abundances. This value is well within the uncertainty limits of our Fe I abundances (see §3.1). Since we have mostly solar-metallicity and mildly metal poor stars in our program, the corrections for NLTE effects were not applied.

Surface gravities were calculated by demanding that Fe I and Fe II lines yield the same mean abundances to within the 1σ internal scatter uncertainties of both species. Finally, we iterated on the $[\text{Fe}/\text{H}]$ metallicities until the values assumed in model creation were consistent with those implied by the line abundance averages. Derived model parameters of our stars are given in Table 3.

We also derived solar abundances (Table 4) applying the same procedure to all the species investigated here. The high-resolution solar data were obtained from the electronic version of the solar center-of-disk spectrum of Delbouille et al. (1973)⁸. These abundances were used for differential determination of the stellar abundances. These differential abundances should give more accurate “internal” results than absolute abundances since many of the systematic errors can be nearly compensated in comparing our stars with the Sun. Our internal solar abundances generally agree with those recommended by Asplund et al. (2009), to within the mutual uncertainties. Nitrogen is the sole exception with a substantial difference, $\sim +0.15$ dex, which potentially could lead to a small offset in our $[\text{N}/\text{Fe}]$ results

⁷ For elements A and B, $[\text{A}/\text{B}] = \log (N_A/N_B)_\star - \log (N_A/N_B)_\odot$ and $\log \epsilon(\text{A}) = \log (N_A/N_H) + 12.0$

⁸ Available at the Bass2000 web site, <http://bass2000.obspm.fr/>

compared to the previous studies that we will consider in §4.3. Our adopted CN oscillator strengths from the Kurucz database may be the major factor contributing to this offset. Exploration of this issue in detail is beyond the scope of our paper.

3.1. Uncertainties in Parameters

The internal uncertainties in atmospheric parameters T_{eff} , $\log g$, and ξ_t were estimated by running a series of trial analyses on the spectral data of BD+27 2057, HD 84686 and HIP 98587. For temperature uncertainties, we varied the assumed T_{eff} in steps of 50 K and kept the other parameters fixed during the analysis. The temperature was changed until the mean abundance difference between low and high excitation Fe I lines exceeded the $\pm 1\sigma$ scatter of individual line abundances derived with the optimal T_{eff} , in other words, until Fe I abundances showed an obviously unacceptable trend with excitation potential. This method yielded an average uncertainty of ~ 150 K for the T_{eff} .

To estimate the external uncertainty in T_{eff} we have searched the literature for previous high-resolution studies of our program stars. We found no large samples in common with our stars, but from the T_{eff} values reported in various publications we have generated Figure 2. The heterogeneity of the literature data does not justify a detailed statistical treatment, but it is clear that our T_{eff} values track those in previous publications, with a scatter of ~ 120 K. We adopt an overall T_{eff} uncertainty of ± 150 K.

Our T_{eff} values for a few stars, however, deviate significantly from previous estimates. Since temperature estimates are critical to assessment of RHB or RC status for our stars, we turned to the spectroscopic “Line Depth Ratio” (LDR) method of T_{eff} determinations. Gray & Brown (2001) showed that simple LDRs of several line pairs in the 6200 Å spectral region (most often a ratio formed by comparing the central depths of a V I and an Fe I line) Their paper maps the LDRs to stellar $B - V$ values and those colors in turn to T_{eff} estimates. LDRs are excellent temperature indicators especially for giants with spectral types between G3 and K3 (see also Figure 7 of Gray & Brown 2001). This method produces effective temperatures well within the uncertainty levels of 150 K and gives us an independent spectroscopic check on our spectroscopic T_{eff} estimates from Fe I lines.

We measured LDRs for our whole sample. We mainly made use of the line ratio pairs recommended by Gray & Brown (2001)⁹ and derived an average $T_{\text{eff}}(\text{LDR})$ for the stars.

⁹The line ratio pairs used for LDR temperatures: V I(6224.5 Å)/Ni I(6223.9 Å) , V I(6233.2 Å)/Fe I(6232.6 Å), V I(6242.8 Å)/Si I(6243.8 Å), V I(6251.8 Å)/Fe I(6252.5 Å),

These line pairs compare the central depths of a very T_{eff} -sensitive transition (almost always a low-excitation V I line) with usually a high-excitation transition of another Fe-group species. We especially made use of the 6224.5 Å/6223.9 Å pair that compares a V I line with $\chi = 0.29$ eV to a Ni I line with $\chi = 4.10$ eV. Their LDR was the most useful because it could be reliably measured throughout most of the T_{eff} domain of our sample. However, the depths of V I lines weaken rapidly with increasing temperature (≥ 5500 K). For example, for the five V I lines recommended by Gray & Brown (2001) for LDR studies, $\langle EW \rangle \simeq 6$ mÅ in the solar spectrum (Moore et al. 1966). Lines with such small EW s are near the reliable detection/measurement limit of our spectra. Therefore for warmer stars of our sample we also measured some LDRs proposed by Strassmeier & Schordan (2000).

A comparison of our spectroscopic and LDR temperatures are given in Figure 3. The error bar depicted in this figure corresponds to the standard deviation of the mean difference between these two temperatures, $\sigma \simeq \pm 150$ K. A change in the correlation is apparent at $T_{\text{eff}} < 5500$ K, which we have highlighted by using different colors for the symbols of stars warmer and cooler than this T_{eff} . Although we see a small systematic bias towards higher temperatures for $T_{\text{eff}} < 5500$ K (Figure 3, purple points), the standard deviation of these points is around 90 K and well within the uncertainty limits. We suggest that this systematic deviation may both arise from the method we adopt from Gray & Brown (2001), which first involves a calibration of LDR against B–V color indices, then converts these into temperatures, and LDRs that we obtained with different instrumentation than those of Gray & Brown (2001). As mentioned above, this temperature is near the reliability limit for the LDR method using these transitions. On the other hand, for $T_{\text{eff}} > 5500$ K, which proves to be the more important domain for identifying true RHB targets, these two T_{eff} estimators are considerably in good agreement. This result suggests that for stars when clashes occur between photometric and spectroscopic temperatures, the photometric values are probably not reliable for $T_{\text{eff}} < 5500$ K. In general, LDR method supports our claimed temperatures for the stars, including the ones which our spectroscopic values clash with literature estimates.

We determined internal uncertainties for $\log g$ and ξ_t through repeated trials with variations in these quantities. The typical average uncertainties were estimated as 0.16 dex and 0.2 km s^{-1} , respectively. Comparison of our $\log g$ results with previously reported ones resulted in an external uncertainty level of ≈ 0.25 dex. By taking into account both internal and external uncertainty levels, we adopt an average uncertainty for $\log g$ of $\approx \pm 0.3$ dex.

We also calculated “physical” gravities and compared them with spectroscopic gravities in order to possibly gain insight on the masses of our stars. We use the following standard

V I(6256.8 Å)/Fe I(6255.9 Å)

equation for physical gravities

$$\log g_{\star} = 0.4(M_{V\star} + BC - M_{\text{Bol}\odot}) + \log g_{\odot} + 4\log\left(\frac{T_{\text{eff}\star}}{T_{\text{eff}\odot}}\right) + \log\left(\frac{m_{\star}}{m_{\odot}}\right).$$

For the Sun, we adopted $T_{\text{eff}} = 5780$ K, $\log g = 4.44$ dex, and $M_{\text{Bol}\odot} = 4.75$ mag. Bolometric corrections were calculated using the relation given by Alonso et al. (1999). A comparison of physical gravities, $\log g(\text{theo.})$, with spectroscopic gravities, $\log g(\text{spec.})$, is given in Figure 4. A significant uncertainty in a physical gravity calculation is the assumed mass. Therefore in the figure we give three $\log g(\text{theo.})$ values calculated for the masses of 1, 2 and 4 M_{\odot} . They are shown with dashed and dotted lines. The best average agreement between these two $\log g$ scales for significantly evolved stars ($\log g \lesssim 3.0$) is for $M \simeq 2 M_{\odot}$ and for MS/SG stars it is $M \simeq 2.5 M_{\odot}$. The joint uncertainties are too large to draw conclusions about individual stars, but does suggest that our sample is not dominated by high mass stars.

In order to derive the effect of these uncertainties on abundance determinations, we did multiple analyses by changing T_{eff} , $\log g$, $[\text{Fe}/\text{H}]$, and ξ_t within their uncertainty limits. The effective temperature uncertainties create an uncertainty around 0.15-0.16 dex in Fe I and the uncertainties in $\log g$ make the Fe II abundances change in less than 0.1 dex. The other elements’ abundances vary in between 0.1-0.16 dex due to T_{eff} uncertainties. In general, the uncertainties in surface gravity and microturbulent velocity result in abundance uncertainties less than $\simeq 0.1$ dex.

Finally we comment on the uncertainties in our derived $^{12}\text{C}/^{13}\text{C}$ ratios. These are nearly insensitive to model atmosphere uncertainties, since ^{12}CN and ^{13}CN are nearly identical molecules. We estimated the $^{12}\text{C}/^{13}\text{C}$ uncertainties by fitting synthetic spectrum to the observed ^{12}CN and ^{13}CN features with various isotopic ratios to estimate their maximum and minimum probable values. The error estimates for the $^{12}\text{C}/^{13}\text{C}$ ratios are given in Table 5.

3.2. Photometric Temperatures and Reddening

Since we observed almost half of our program stars at high spectral resolution for the first time, our sample lacked a consistent set of reported atmospheric parameters. This made it difficult to have meaningful temperature estimates to start our analyses, so we relied exclusively on our Fe I line analyses to derive T_{eff} values, augmenting these with LDR estimates. Armed with these results we now compare spectroscopic and photometric temperatures for the stars in common. We concentrate on the $V - K$ color because it is one of the best photometric temperature indicators, having almost no dependence on metallicity

and gravity (e.g. Alonso et al. 1999, Ramírez & Meléndez 2005). The V magnitudes that we employ are on the standard Johnson photometric system; the K_s magnitudes are from the Two Micron All Sky Survey. We adopt the $(V - K_s)$ - T_{eff} calibration equation from Ramírez & Meléndez (2005).

Before calculating the photometric T_{eff} values, we first applied interstellar reddening corrections to the $V - K_s$ colors. A recent survey of the regions within 300 pc of the Solar System showed that the “Local Bubble” (Lallement et al. 2003) has a shape of an irregular lacuna, which extends ~ 60 pc towards the Galactic center, 80–150 pc towards the outermost edge of the Galaxy and ~ 200 pc above and below the Galactic plane. But ISM dust extinction is patchy and varies considerably toward different sightlines, and many of our stars have poorly-constrained distances. Therefore we estimated their reddening in three different ways. In all cases, we adopted a typical Local Bubble radius of 75 pc and assumed no reddening for stars estimated to be within that distance (e.g. Henry et al. 2000).

For our first reddening estimate, we have applied an isotropic reddening correction for the stars have distances $75 < d \leq 300$ pc, adopting $A_v = 0.8$ mag kpc $^{-1}$ (Henry et al.). The extinction values of eight stars with distances $d > 300$ pc were obtained from the NASA/IPAC Extragalactic Database (NED)¹⁰ extinction calculator. Zero reddening was assumed for the stars with high Galactic latitudes, $|b| \geq 50^\circ$ (e.g, Sandage 1972). For the second and third reddening estimates, we employed the methods described by Chen et al. (1998) and Hakkila et al. (1997). Our computations with the latter method used Hakkila’s EXTINCT code¹¹ which takes into account various interstellar extinction correction methods from several studies (see Hakkila et al. for more details).

We applied each of these reddening estimates to the observed $V - K$ colors, computed photometric temperatures from the reddening-corrected $V - K$ colors using the Ramírez & Meléndez (2005) formula, and correlated them with our spectroscopic temperatures as shown in Figure 5. Inspection of this figure clearly suggests that the two T_{eff} scales are well correlated, and that various reddening assumptions produce little substantive variations in the temperature correlations. Therefore, we have adopted our $E(B - V)$ values for reddening for the entire sample.

¹⁰ <http://ned.ipac.caltech.edu/>

¹¹ Available at <http://ascl.net/extinct.html>

4. ABUNDANCE DETERMINATIONS

Using the model atmospheres given in Table 3, we determined abundances of several elements in our program stars. We report these as relative abundance ratios $[X/H]$ in Table 7. Whenever possible, we computed the abundances from line EWs. For complex transitions, those that have significant hyperfine and isotopic substructure, and those that have significant line blending issues, we resorted to synthetic/observed spectrum matches to determine the abundances. We were especially interested in three element groups that could help constrain the Galactic population memberships of our stars and verify their evolutionary states. In the following subsections we consider in turn the α , the neutron-capture, and the proton-capture element groups.

4.1. α -Elements: Silicon and Calcium

The abundances of α -elements exhibit the same behavior in giant and dwarf stars of solar metallicity ($[\alpha/Fe] \sim 0$; Soubiran & Girard 2005, Mishenina et al. 2006). In thick disk main-sequence and subgiant stars, the α elements typically become overabundant as metallicity decreases, reaching $[\alpha/Fe] \sim +0.3$ at $[Fe/H] \sim -1$ (e.g. Tautvaišienė et al. 2001, Tautvaišienė et al. 2001, Reddy et al. 2006). The temperatures and gravities of these prior large samples are $5000 \text{ K} \lesssim T_{\text{eff}} \lesssim 6500 \text{ K}$ and $3.4 \lesssim \log g \lesssim 4.7$. Less systematic abundance trend information is available for thin/thick disk giant stars, which in our case cover the approximate parameter range $4800 \text{ K} \lesssim T_{\text{eff}} \lesssim 5600 \text{ K}$ and $2.2 \lesssim \log g \lesssim 4.0$.

The easily-observable α elements are Mg, Si, and Ca. Often Ti is grouped with the other α 's due to its similar abundance behavior with metallicity. However, Ti is not a pure α element because its dominant isotope is $^{48}\text{Ti}_{22}$, which is not an even multiple of α particles. Here we concentrated on Si and Ca abundances, since they have large numbers of transitions with a range of line strengths in the yellow-red spectral region (most Mg I lines are very strong in our G-K giant stars). We generally used about 9 Si I and 15 Ca I lines, and derived abundances from their EWs.

We compare our Si and Ca abundances with published values in Figure 6. The literature data are taken from several studies that are given in the figure caption: Tautvaišienė et al. (2001), Reddy et al. (2003), Bensby et al. (2003), Reddy et al. (2006) and Mishenina et al. (2006). Our sample has a wide metallicity range $-1.0 \leq [Fe/H] < +0.5$ and it is clear that the α elements behave similarly in our cooler giants as they do in warmer main sequence stars and subgiants. Even though slight scaling differences (< 0.1 dex) naturally result from different solar abundances, different line choices, and different oscillator strengths adopted

here compared with previous studies, our results are generally in good agreement with the literature. At a given $[\text{Fe}/\text{H}]$ metallicity our mean $[\text{Ca}/\text{Fe}]$ values are typically within 0.05 dex of literature values, and $[\text{Si}/\text{Fe}]$ are within 0.01 dex.

4.2. Neutron-Capture Elements

Among thin and thick disk stars, those elements whose solar-system origin is due chiefly to “slow” neutron bombardment reactions (the *s*-process; e.g. Sr, Y, Zr, Ba, La, and Ce) generally exhibit their solar abundance ratios ($[\text{X}/\text{Fe}] \sim 0$) throughout metallicity regime $-1.0 \lesssim [\text{Fe}/\text{H}] \lesssim +0.2$. But those elements that are products of “rapid”-blast neutron capture events (the *r*-process; Eu, Gd, Dy) tend to increase in relative abundance with decreasing metallicity. The most easily-observed *r*-process element is Eu, and its mean abundances reaches $[\text{Eu}/\text{Fe}] \sim +0.4$ at $[\text{Fe}/\text{H}] \sim -1$. A good summary of the disk *s*- and *r*-process abundance trends can be seen in Figure 17 of Reddy et al. (2006). Additionally, Simmerer et al. (2004) has shown that a distinct kinematic signature in disk neutron-capture elements: stars with larger space motions have often much lower *s*-process abundances than *r*-process ones (see their Figure 12).

There are not a lot of useful neutron-capture element ($Z > 30$) transitions in the yellow-red spectral region. We considered just La (75% *s*-process origin in solar-system material, e.g., Sneden et al. 2008 and references therein), and Eu (97% *r*-process).

La II: transitions at 6262.2 and 6390.5 Å can be detected in nearly all of our stars. These lines have well-determined transition probabilities and hyperfine structure parameters (Lawler et al. 2001a; see also Ivans et al. 2006 for complete substructure line lists for these transitions). The sole naturally-occurring isotope of this element is ^{139}La . Because of the complexity of these La II transitions we used synthetic spectrum analyses to determine the abundances. Notable contaminants to the La features are CN red-system lines, but in most cases the CN strengths were small and did not materially affect the derived abundances.

Eu II: transitions at 6645.1 and 7217.5 Å were used in the Eu abundance analyses. The transitions are very complex, because Eu has both hyperfine and isotopic substructure. There are two Eu stable isotopes, ^{151}Eu (48% of the total solar-system Eu abundance) and ^{153}Eu (52%). There is little difference in Eu isotopic ratios generated in *r*-process and *s*-process environments. Spectroscopic studies of Eu II in extremely metal-poor, Eu-enhanced stars suggest that the ^{151}Eu fraction is $\approx 50\%$ for *r*-rich stars (Sneden et al. 2002, Aoki et al. 2003a, Roederer et al. 2008) and $\approx 57\%$ for *s*-rich stars (Aoki et al. 2003b). Therefore in our Eu syntheses we adopted the solar-system isotopic ratios. The basic laboratory analyses of

these lines were published by Lawler et al. (2001b); full hyperfine/isotopic substructure lists are in Ivans et al. (2006).

The abundance variations for La II and Eu II as a function of metallicity are given in Figure 7. The observed trends (no apparent change in $[\text{La}/\text{Fe}]$, increasing $[\text{Eu}/\text{Fe}]$ at lower metallicities) are in complete agreement with previous results cited above. The neutron-capture element abundances, combined with those of the α elements clearly provide Galactic population indicators for our stars.

4.3. The Proton-Capture Abundances

Evolved Population I solar-metallicity stars show evidence of convective envelope mixing; their observed light elements Li, C, N, and O clearly have been altered via interior synthesis in $p - p$ and CNO cycles. The original C abundance drops by a factor of about two, the N abundance rises by comparable amounts, and the carbon isotopic ratio drops to values usually between 15–30 (e.g. Lambert & Ries 1981). Mildly metal-poor, high-velocity stars (thick disk, labeled old disk in early papers) of about a solar mass have lower $^{12}\text{C}/^{13}\text{C}$ ratios but less evidence for depleted C and enhanced N (e.g., Cottrell & Sneden 1986). Low mass giant stars of the Galactic halo often display more dramatic $^{12}\text{C} \rightarrow ^{13}\text{C}$ and $\text{C} \rightarrow \text{N}$ conversions (e.g., Gratton et al. 2000). Thus the CNO abundances of evolved stars can yield information on their internal evolutions and population memberships.

Since stars easily destroy Li in relatively low-temperature proton-capture reactions, Li abundances or upper limit estimates in metal-rich stars provide additional information. The presence of Li in the spectrum of an evolving star usually suggests that envelope convection has not yet developed to a point where dredge-down of original surface Li has effectively cleaned it from the star’s envelope. The absence of Li can indicate (but not always) that other proton-capture products may have been dredged up to the surface. This straightforward interpretation is complicated by the relatively rare phenomenon of Li-rich giants (e.g., Charbonnel & Balachandran 2000, Kumar et al. 2011 and references therein). This increases the importance of searching for this element in the spectrum of any evolved star.

Unfortunately, many atomic and molecular transitions that are CNOLi abundance indicators have significant detection and/or analytical issues. Here we describe the transitions that we used, and our atomic/molecular parameter choices.

C I: High excitation ($\chi \gtrsim 7.7$ eV) lines of this species are strong in the warmest candidate stars but weaken with decreasing T_{eff} . We adopted the transition probabilities for these lines

recommended in the NIST Atomic Spectra Database (Ralchenko et al. 2011)¹². However, the C I lines decrease in strength so quickly with decreasing T_{eff} , often only a couple of them could be used for C abundances in our stars.

CH G-Band: We also employed the CH $X^2\Pi - A^2\Delta$ “G-band” to derive C abundances via spectrum syntheses. Significant G-band absorption occurs in the 4200–4400 Å spectral range, and we estimated C abundances from three regions (4300–4308 Å, 4308–4315 Å, and 4322–4327 Å) and averaged the results. The 4308–4315 Å region proved to be the most reliable C abundance indicator, due to greater atomic-line contamination in the other two spectral regions. The synthetic spectrum line list was formed with ^{12}CH and ^{13}CH lines from Plez (private communication; see, e.g., Hill et al. 2002, Plez & Cohen 2005) and atomic lines from the Kurucz (2011) compendium. The CH lines are plentiful and relatively strong throughout the atmospheric parameter domain of our program stars. As an example of the CH observed/synthetic spectrum matches, we show in Figure 8 the 4308–4315 Å spectral region in a typical program star. Generally more reliable C abundances were obtained from the CH band syntheses than those from the C I EW measurements, especially among the cooler ($T_{\text{eff}} < 5500$ K) stars.

CN: We used synthetic spectrum calculations of ^{12}CN and ^{13}CN $A^2\Pi - X^2\Sigma$ red system lines in the 7995–8040 Å region to determine N abundances and $^{12}\text{C}/^{13}\text{C}$ ratios. The synthesis line lists were taken from Kurucz (2011). A triplet of ^{13}CN lines near 8004.7 Å was the primary $^{12}\text{C}/^{13}\text{C}$ indicator, but several other, usually weaker features (e.g., at 8007.9, 8010.4 and 8011.2 Å) were used for confirmation. In Figure 9, we give an example of a synthetic spectrum fit to the ^{12}CN and ^{13}CN features in the 8002.5–8011.5 Å region. Derived $^{12}\text{C}/^{13}\text{C}$ ratios for our program stars are given in Table 5. C-N-O abundances are bound to each other through molecular equilibrium, which becomes more important towards lower temperatures. The accuracy of N abundances especially depend on the accuracy of C abundances through CN formation. Note that our line list produced a systematic offset of ~ 0.15 in the solar N abundance (Table 4) compared to Asplund et al. (2009). This would suggest that perhaps we have an offset of about +0.15 dex in our N abundances.

[O I]: There are two ground-state forbidden transitions upon which are based most of the O abundances in red giant stars. We analyzed only the 6300.3 Å; its companion at 6363.8 Å is much weaker and suffers from large amounts of CN contamination. The 6300 Å line has a very accurate transition probability (Allende Prieto et al. 2001 and references therein). The 6300 Å [O I] line is blended with a Ni I line at 6300.34 Å; see Allende Prieto et al. One needs to remove its contribution carefully during the modeling of the [O I] spectral region

¹² Available: <http://physics.nist.gov/asd3>

around 6300 Å. Of some importance is the Ni I oscillator strength; we use the value given by Johansson et al. (2003).

O I: In the spectra of our warmer stars the forbidden line is too weak to yield reliable abundances, so we also used the often-analyzed very high-excitation 7770 Å triplet. For these lines we adopted gf -values from the NIST database (Ralchenko et al. 2011). Unfortunately, it is well known that the O I triplet lines are subject to NLTE effects, in the sense that their LTE-based abundances are always too large ($\lesssim 0.2$ dex, Gratton et al. 1999, Bensby et al. 2004) compared to abundances from the forbidden lines. In order to correct for the NLTE effects, we followed a similar approach to the NLTE-correction method of Bensby et al. (2004). That is, we applied a “robust regression” analysis and derived the following equation for $[\text{O}_{6300}/\text{O}_{7774}]_{\text{cor}}$ as a function of T_{eff} , $\log g$ and $[\text{Fe}/\text{H}]$:

$$\begin{aligned} [\text{O}_{6300}/\text{O}_{7774}]_{\text{cor}} = & -0.293(\pm 0.027) + 0.429(\pm 0.839) \cdot \log\left(\frac{T_{\text{eff}\star}}{T_{\text{eff}\odot}}\right) \\ & - 0.232(\pm 0.033) \cdot \log\left(\frac{\log g_{\star}}{\log g_{\odot}}\right) \\ & + 0.136(\pm 0.055) \cdot [\text{Fe}/\text{H}] \end{aligned}$$

Here, $[\text{O}_{6300}/\text{O}_{7774}]_{\text{cor}}$ represents the difference between the oxygen abundances gathered from the $[\text{O I}]_{6300}$ line and the $[\text{O I}]_{7774}$ triplet lines. Then we simply subtracted this difference from $[\text{O}/\text{H}]_{7774}$ abundances in order to obtain NLTE-corrected $[\text{O}/\text{H}]_{7774}^{\text{NLTE}}$ values. In Figure 10, we compare the deviation of the differences between $[\text{O}_{6300}/\text{O}_{7774}]_{\text{LTE}}$ and $[\text{O}_{6300}/\text{O}_{7774}]_{\text{NLTE}}$. The mean and the standard deviation of the correlation after correction are 0.05 dex and $\sigma \simeq \pm 0.12$ dex, respectively.

In Figure 11, we plot our CNO abundances along with previously reported values, using the same comparison samples. While the derived mean O and N abundances of our stars are in good agreement with literature mean values at similar metallicities, our C abundances are somewhat lower those from previous studies. But the comparison samples in this case are not the best, because the literature data are dominated by main sequence and subgiant stars, while our program stars are clearly much more evolved. Therefore in Figure 12 we repeat the exercise of the previous figure, but with two differences. First, we have eliminated the stars of our sample that are probably not chemically mixed (those with $T \gtrsim 5400$ K and/or $\log g \gtrsim 3.5$). Second, we added literature CNO abundance results only from studies that concentrated on red giant stars. Our C abundances are more in accord with those in other samples of evolved giants.

Thick disk giants ($[\text{Fe}/\text{H}] < -0.25$) in general show higher C and O abundances than their thin disk counterparts. The O enrichment is indicative of larger Type II SNe contributions to thick disk than thin disk stars, combined with no depletion in ON-cycle H-fusion

(interior temperatures are too low) in the low-mass thick-disk giants that we observe. The higher C in thick disk stars suggests that the lower-metallicity, relatively low-mass thick-disk giants have relatively shallow convective envelopes, and dredge-up has failed to reach the interior fusion zones where the CN-cycle has run to completion. This echos the discussion in Cottrell & Sneden 1986, who concluded that in their old disk giants, “only the coolest (outer) portions of the CNO-processed hydrogen burning shell, where $^{12}\text{C}(p, \gamma)^{13}\text{C}$ has taken place, have been convectively mixed into outer layers”. Theoretical support for this notion was given in Sneden et al. (1986), whose Table 6 gives D. A. Vandenberg’s predicted C/N ratios from standard evolutionary model stars that have experienced first dredge-up. It is clear that as mass and metallicity decrease, model stars exhibit decreasing surface C and N abundance changes.

Li I: Unless the Li abundance is extraordinarily large, only the 6707.8 Å resonance line of the neutral species can be detected in cool stars. This ground-state doublet transition has a well-determined gf value; see the summary of experimental and theoretical studies in Smith et al. (1998). The transition is complex, with both isotopic and hyperfine substructure. We adopted the parameters given in the line compendium of Kurucz (2011)¹³.

We were able to measure Li I abundances for some of our targets (see Table 6). Since Li line strength is a severe function of T_{eff} , for stars with undetectable Li here are approximate abundance upper limits as guidelines for interpretation: for stars with $\log g \geq 3.5$ and $T \geq 5500$, $\log \epsilon(\text{Li}) < 1$, and for those with $\log g < 3.0$ and $T \leq 5100$, $\log \epsilon(\text{Li}) < +0.5$ (with the limit of course decreasing towards lower temperatures). The Li abundances decrease as T_{eff} and $\log g$ decrease. This is as expected in normal stellar evolution: during the path from main sequence to red giant phases, the deepening convective envelopes bring Li down from the surface layers where it can be destroyed easily at relatively low fusion-zone temperatures. Program stars with higher surface Li abundances have undetectable ^{13}C , consistent with their chemically un-evolved status. Six stars of our sample have low $^{12}\text{C}/^{13}\text{C}$ values, but detectable Li I lines; these all appear to be plausible RHB and RC candidates (see Table 7). For these stars, $\langle \log \epsilon(\text{Li}) \rangle \sim 0.8$. Standard evolution models (e.g., those without extra mixing mechanisms seeming needed for Population II giants) predict surface Li depletion by factors up to about 30 (Iben 1967a). If a star begins main-sequence life with the present interstellar medium Li abundance ($\log \epsilon(\text{Li}) \sim +3.0$, e.g. Grevesse & Sauval 1998) then through ordinary stellar evolution it should exhibit $\log \epsilon(\text{Li}) \lesssim +1.5$. None of our evolved program stars have Li abundances near to this value, indicating either that their natal Li contents were not as high as the present ISM value, or that extra mixing during their lives

¹³<http://kurucz.harvard.edu/linelists.html>

destroyed Li beyond the standard predictions.

5. KINEMATICS

Among the overall sample of 76 stars, we have distance information for 58 of them to facilitate a kinematical investigation. In order to calculate stellar space velocities, we have collected parallaxes and proper motions, as well as their errors, from van Leeuwen (2007), who recently published new reduction results of HIPPARCOS data. We either adopted the RVs already available in the literature or we measured new values as described in §2.2. We used the matrix equations given by Johnson & Soderblom (1987) and calculated the Galactic velocity components U_{LSR} (positive toward the Galactic center, V_{LSR} (positive in the direction of the Galactic rotation), W_{LSR} (positive toward the NGP), and their uncertainties ($\sigma_{U_{\text{LSR}}}$, $\sigma_{V_{\text{LSR}}}$, $\sigma_{W_{\text{LSR}}}$) with respect to the Local Standard of Rest (LSR). Correction for the solar motion was made by adopting the values $(U, V, W)_{\odot} = (+10.00, +5.25, +7.17)$ from Dehnen & Binney (1998). The results are given in Table 8.

In Figure 13 we show these kinematics in a Toomre diagram. This kind of plot gives the kinematical distribution of the stars in terms of their combined vertical and radial kinetic energies as a function of their rotational energies. The solid curves of Figure 13 are lines of constant total space velocity, $V_{\text{tot}} = (U_{\text{LSR}}^2 + V_{\text{LSR}}^2 + W_{\text{LSR}}^2)^{1/2}$. The dashed line represents the $V_{\text{tot}} = 70 \text{ km s}^{-1}$, which approximately separates the thin and thick disk populations of the Galaxy (e.g. Bensby & Feltzing 2009, Nissen 2004). Stars with total space velocities of $70 < V_{\text{tot}} < 180 \text{ km s}^{-1}$ are considered to be probable thick disk, those in the range $50 < V_{\text{tot}} < 70 \text{ km s}^{-1}$ are called transition (thin/thick) objects, and those with $V_{\text{tot}} < 50 \text{ km s}^{-1}$ are probable thin disk members of the Galaxy.

Inspection of Figure 13 reveals that our sample is dominated by thin disk stars. Out of 58 stars with kinematic information, 39 (the squares) probably reside in the thin disk, 10 probably are in the thick disk, and 9 are kinematic transition objects whose thin/thick status is ambiguous. In Figure 13 we also use filled and open version of the symbols to indicate the detection status of ^{13}CN features in individual stars: those with $^{12}\text{C}/^{13}\text{C} < 30$, and those with no detection of ^{13}CN (thus $^{12}\text{C}/^{13}\text{C} > 30$), respectively. We will consider the carbon isotopic ratio distribution further in §7.

Looking at the kinematics of our stars in more detail, in Figure 14 we show the correlations between total space velocity V_{tot} and eccentricity, and between the velocity component of W_{LSR} and eccentricity. The eccentricities were calculated using the method described in Dinescu et al. (1999). The solar circle radius of $R_0 = 8.0 \text{ kpc}$ around the Galactic center and

an LSR rotation velocity of $\Theta = 220 \text{ km s}^{-1}$ were adopted. As expected, the total velocity is strongly correlated with eccentricity in our sample. However, the relationship between the vertical velocity and eccentricity is not obvious beyond increased scatter in V_{tot} at large eccentricities. Several of our thick disk stars have low $|W_{\text{LSR}}|$ velocities ($\lesssim 20 \text{ km s}^{-1}$). Given that W_{LSR} is proportional to z_{max} , the maximum vertical distance of a star to the Galactic plane, these particular stars with W_{LSR} apparently reside close to the Galactic plane.

The space motions and derived metallicities of our program stars are related. In Figure 15, we plot the three space velocity components against $[\text{Fe}/\text{H}]$ in panels (a), (b), and (c). The larger dispersions of the U_{LSR} , V_{LSR} , and W_{LSR} velocities in the true thick-disk stars is clear from inspection of these panels. Useful velocity limits in order to separate the thin and thick disk stars appear to be $|W_{\text{LSR}}| \approx +20 \text{ km s}^{-1}$ and $V_{\text{LSR}} < -40 \text{ km s}^{-1}$. However, all three velocity components that comprise total space velocity must be taken into account in assessing the Galactic membership of individual stars. In panel (d) of Figure 15 we plot $[\text{Fe}/\text{H}]$ versus eccentricity, and it is clear that lower metallicity stars in our sample generally have more eccentric orbits. This is similar to the relation recently suggested by Lee et al. (2011). However, their study considered only thick-disk stars with subsolar metallicities ($[\text{Fe}/\text{H}] < -0.3$). We stress here that stars with thick-disk kinematics (including eccentricity) but $[\text{Fe}/\text{H}] > -0.3$ have no obvious metallicity-kinematics connections.

In Figure 16 we explore the relationship between our α -element abundances ($[\alpha/\text{Fe}] = ([\text{Ca}/\text{Fe}] + [\text{Si}/\text{Fe}])/2$), metallicity, and kinematics. In panel (a) we correlate $[\text{Fe}/\text{H}]$ with $[\alpha/\text{Fe}]$. The well-documented rise in relative α -element abundances with decreasing metallicity in disk populations is reproduced in our relatively small sample. All of our thick-disk stars with $[\text{Fe}/\text{H}] < -0.3$ have $[\alpha/\text{Fe}] \gtrsim +0.2$. Although our sample is small, there seems to be a clear separation between the thick and thin disk stars for the metallicities of $[\text{Fe}/\text{H}] < -0.3$ as indicated in larger surveys (e.g. Reddy et al. 2006). Stars with $[\text{Fe}/\text{H}] > -0.3$ show similar $[\alpha/\text{Fe}]$ ratios regardless of their membership either in the thick or the thin disk. In panel (b) we plot the $[\alpha/\text{Fe}]$ versus metallicity. This relationship can be compared with the W_{LSR} versus $[\text{Fe}/\text{H}]$ plot shown in panel (d) of Figure 15. They tell essentially the same story, linking in our sample the kinematics, metallicities, and α -element abundances of our sample.

6. EVOLUTIONARY STATUS

We estimated the probable evolutionary stages of our program stars by taking into account their loci in the $T_{\text{eff}}\text{--}\log g$ plane, their absolute magnitudes (luminosities), and their $^{12}\text{C}/^{13}\text{C}$ values derived from our spectral analysis. In Figure 17 we show the $T_{\text{eff}}\text{--}\log g$

diagram, using different symbols to denote stars with and without detected ^{13}CN spectral features. Although we selected our targets as luminosity class–III stars, our atmospheric analyses revealed about 1/3 of our sample to be either MS or SGB stars. These are evident in the figure as higher temperature, higher gravity stars with weak/absent ^{13}CN .

In Figure 17 we have also shown theoretical evolutionary tracks from Bertelli et al. (2008) ($Y=0.26$, $Z=0.02$; note that we do have a few low metallicity stars in our sample but for simplicity we plot only tracks with a single metallicity). The evolutionary-track masses displayed here are from 0.8 to 3 M_{\odot} . For tracks with 0.8–2 M_{\odot} the evolutionary phases go up to RGB tip (at lower temperatures than displayed here), while the 2.5 and 3 M_{\odot} tracks proceed up to the first thermal pulse stage. The base of the RGB, including masses up to 4 M_{\odot} , is also shown with a dashed line, which is constructed from the data of Bertelli et al. (2008). We have also included HB evolutionary tracks for the mass range 0.55–2 M_{\odot} (denoted by the thick black lines). Only 0.55 M_{\odot} HB track evolves up to the early AGB phase. Other HB tracks start from the zero-age horizontal branch (ZAHB) and go up to the maximum He-burning phase. HB tracks with masses higher than 0.55 M_{\odot} make an *arc* shape in Figure 17. This arc covers a temperature range $4500\text{ K} \lesssim T_{\text{eff}} \lesssim 4900\text{ K}$, and thus essentially defines the RC region. RC stars are the reddest HB stars with higher masses than normal RHB stars. Both of them are at the core He-burning stage and all belong to the RHB class in general.

In §3.1 we compared spectroscopic surface gravities with theoretical ones (Figure 4), suggesting that, for most of our targets, the masses are $\sim 2M_{\odot}$. This is consistent with the inferred evolutionary-track masses of the warmer ($T_{\text{eff}} > 5300\text{ K}$), higher gravity ($\log g > 3.0$) stars in Figure 17. The SG stars should not yet have convectively-mixed envelopes, so it is not surprising that these objects also do not have detectable ^{13}CN lines and hence $^{12}\text{C}/^{13}\text{C} > 30$ (e.g. Thorén et al. 2004).

For almost all of the stars with $T_{\text{eff}} < 5300\text{ K}$, the masses inferred from the evolutionary tracks in Figure 17 are $\gtrsim 3 M_{\odot}$. These implied masses are much larger than those of the warmer MS/SG program stars, and also are inconsistent with our earlier (§3.1) assertion that almost all of our stars have actual masses $\lesssim 2 M_{\odot}$. The implication is that our lower temperature stars are not SG stars on their first ascent up the RGB, but instead are post-RGB stars in the helium-burning RHB evolutionary stage. It is possible for RHBs to be confused with high-mass SGs, which can have similar absolute magnitudes to the RHBs. But such SG stars should be rare because the timescales for passage of $\gtrsim 3 M_{\odot}$ stars through the 4800–5300 K temperature domain ($\sim 10^5$ – 10^6 years) are short compared to the RHB He-burning timescales ($\sim 10^8$ years) of less massive (thus probably more plentiful) stars. Our cooler program stars in general ought to be true members of the field RHB population.

For each program star we have estimate a probable evolutionary stage, taking into account its position in the $T_{\text{eff}}\text{-log } g$ plane from arguments presented above, its absolute magnitude when parallax data are available, and its $^{12}\text{C}/^{13}\text{C}$ ratio. These estimates are given in the last column of the Table 7. We suggest that there are 18 RHB stars in our sample (5 thick disk and 13 thin disk), along with several RC and RC/RHB stars, most of them members of the thin disk.

7. SUMMARY AND DISCUSSION

In this study we have determined atmospheric parameters and chemical compositions of field RHB candidates selected simply from their colors and absolute magnitudes. The original goal was to increase the sample size of bona-fide RHB stars, and to try to understand the physical processes involved in the existence of these relatively rare highly-evolved objects. We deliberately avoided kinematic biases by employing only photometric and spectral type information in selecting stars for observation.

We gathered high resolution, high S/N spectra of 129 candidate field RHB stars. Preliminary analyses eliminated 53 candidates from further consideration because they proved to be anomalously broad-lined rapidly rotating stars, or double-lined spectroscopic binaries, or stars for which we could not deduce reliable atmospheric parameters. For the remaining 76 program stars, we first determined values of T_{eff} , $\log g$, ξ_t , and $[\text{Fe}/\text{H}]$. Then we derived abundances for α elements Si and Ca, neutron-capture elements La and Eu, proton capture elements Li, C, N, and O. We also determined $^{12}\text{C}/^{13}\text{C}$ isotopic ratios, because detection of ^{13}C provides strong evidence of CN-cycle H-fusion and mixing associated with evolved stars. The derived fundamental stellar parameters T_{eff} and $\log g$, along with the $^{12}\text{C}/^{13}\text{C}$ isotopic ratios, were used to estimate the evolutionary stages of our program stars. This evaluation suggests that about 20% of 76 program stars are true RHB members.

We then computed space velocity components for all of the program stars with available distances, proper motions, and radial velocities (either from the literature or from our own spectra). For each star we estimated Galactic population membership (thin disk, thick disk, and thin/thick transition) only from the kinematics. We examined correlations between kinematics and (a) overall metallicity, and (b) relative abundance ratios of the α elements (confirming these with abundance ratios of the neutron-capture elements). Even with our relatively small sample we recovered well-known differences between thin and thick disk stars. Our thick disk stars have higher space velocities and orbital eccentricities, lower metallicities, and larger α -element ratios than do their thin disk counterparts.

We did not take into account the kinematical constraints during the sample selection, and our moderately small survey of 76 RHB candidates turns out to contain only five probable thick disk stars. These five true thick disk RHBs are very similar to others already identified in the literature (e.g. Cottrell & Sneden 1986, Tautvaišienė et al. 2001): they are mildly metal-poor, α -enhanced (including high oxygen) stars that have low $^{12}\text{C}/^{13}\text{C}$ ratios. They also show little evidence for carbon depletion, as discussed in §4.3. Such stars have relatively low masses, and their appearance on the RHB (instead of the RC) is not surprising: mildly metal-poor globular clusters have well-populated RHBs.

A perhaps more interesting result is that our identified RHB sample is dominated by thin disk, high metallicity stars. These stars, with $T_{\text{eff}} > 5000$ K, are too hot to be RC stars, which have temperatures lower than 4900 K. They also have evolved-star gravities: $\log g = 2.2\text{--}2.8$, substantially smaller than the gravities of subgiants and main-sequence stars (Figure 17). They show no obvious α and neutron-capture abundance anomalies compared to other thin-disk samples. Their proton-capture abundances are unremarkable compared to normal thin-disk RGB stars. In particular, they exhibit $[\text{O}/\text{Fe}] \sim 0$ and $[\text{C}/\text{Fe}] \sim -0.4$, and often low $^{12}\text{C}/^{13}\text{C}$ values, all consistent with expectations from past studies. But their residence in the RHB cannot be easily understood through standard stellar evolution considerations.

Both thick and the thin disk RHBs have a range of $^{12}\text{C}/^{13}\text{C}$ ratios ranging from 5 to 30 (Table 7). Before discussing the $^{12}\text{C}/^{13}\text{C}$ ratios of our stars in detail, we review the physical processes that can affect $^{12}\text{C}/^{13}\text{C}$ ratios during stellar evolution in the next paragraphs.

As a low mass star ($< 2.25 M_{\odot}$) evolves past the MS and SG evolutionary stages, the first dredge-up starts at the base of the RGB (e.g. Iben 1964, 1965, 1967b), accompanied by convective envelope expansion towards inner layers of the star. This will bring CN-cycle processed material up to the outer layers, thus, resulting in surface abundance alterations of the LiCNO group. Fragile Li is severely depleted first. As the convection extends into deeper inner regions, it passes through the transition region which separates the region of ^{12}C converted into ^{14}N . In standard dredge-up theories, mixing of the processed and unprocessed elements results in depletion of surface ^{12}C , lowering the $^{12}\text{C}/^{13}\text{C}$ ratio to $\sim 20\text{--}30$ from its (assumed) initial solar value of ~ 90 (Charbonnel 1994, Charbonnel et al. 1998, Gratton et al. 2000), while the surface ^{14}N values increase. First dredge-up phenomenon leaves a mean molecular gradient (μ -barrier) behind which prevents further mixing (e.g, Charbonnel et al. 1998).

However, previous observational studies have shown that $^{12}\text{C}/^{13}\text{C}$ ratios as low as the CN-cycle equilibrium value of 3.4 (e.g. Sneden et al. 1986, Cottrell & Sneden 1986, Gratton et al. 2000, Tautvaišienė et al. 2001), which obviously requires a non-canonical mixing process during the RGB phase. Recent stellar evolution studies have attempted to solve

this extra-mixing problem by offering physical mechanisms such as rotation-induced mixing (Zahn 1992), cool bottom processing (CBP, Boothroyd & Sackmann 1999) and thermohaline instability plus rotation–induced mixing (Charbonnel & Zahn 2007, Charbonnel & Lagarde 2010). These ideas provide an extra-mixing process that sets in after the “ μ –barrier elimination” which occurs after the convective envelope base recedes towards the surface. Then the H-burning shell eliminates the composition discontinuity left by the convective envelope and enables extra-mixing processes to come into play. For low mass stars, this stage of evolution is also called the “RGB luminosity function bump (LFB)” (Gratton et al. 2000, Charbonnel & Lagarde 2010) at which the H-burning shell burns the newly supplied fuel as it expands outwards. This stage slows down the evolution and causes a temporary luminosity drop along the RGB. For solar metallicities and initial masses of $\leq 2.25 M_{\odot}$ LFB appears at effective temperatures lower than 4800 K (e.g. Charbonnel & Balachandran 2000, Monaco et al. 2011).

As is seen in Figure 17, the evolved stars of our sample (thick+thin disk) are located approximately between 4800–5400 K in T_{eff} and 2.2–2.8 in $\log g$. The stars illustrated with filled circles have low $^{12}\text{C}/^{13}\text{C}$ values (≤ 20) and they clearly reside far away from LFB. We suggest that the stars with especially low isotopic ratios, $^{12}\text{C}/^{13}\text{C} \leq 10$, may have evolved from lower initial masses and undergone a major extra-mixing processes when they passes the LFB. The amount of the extra-mixing is related to both the initial mass and the metallicity of the star, which may explain the deviation in the $^{12}\text{C}/^{13}\text{C}$ values (≤ 20).

Stars have masses higher than $2.25 M_{\odot}$ ignite their central He before the core becomes degenerate. The H-burning shell which surrounds the He-burning core remains until the second dredge-up and never reaches the region of molecular discontinuity left by the convective envelope during the first dredge-up phase. That is why, stars with high initial masses are not expected to show the indicators of extra-mixing, such as low $^{12}\text{C}/^{13}\text{C}$ ratios (Charbonnel 1994, Charbonnel et al. 1998, Charbonnel & Zahn 2007). In our sample, we have evolved stars with $20 < ^{12}\text{C}/^{13}\text{C} < 30$, which are close to the values suggested by canonical models (e.g. Schaller et al. 1992, Charbonnel 1994). These stars are shown with (blue) crosses in Figure 17. Assuming that these stars did have on average larger initial masses than the stars with low isotopic ratios, then the isotopic ratio issue is “solved”, but leaves a problem: why are these stars now in the RHB domain instead of the RC? Here we suggest, but cannot prove, that the RHB stars with higher $^{12}\text{C}/^{13}\text{C}$ ratios have undergone substantial mass loss at some stage(s) of their evolution, leaving them with smaller present envelope masses. Such stars will appear bluer (hotter) than RC stars.

For further insight in Figure 18 we correlate $^{12}\text{C}/^{13}\text{C}$ ratios and $[\text{Fe}/\text{H}]$ metallicities. We include our RHB, RC, and RC/RHB stars along with the data obtained by Lambert & Ries

(1981), Cottrell & Sneden (1986), Gratton et al. (2000) and Tautvaišienė et al. (2001) for the same temperature, luminosity and surface gravity range (same evolutionary stages). We have excluded SG stars and upper RGB stars in this plot. In Figure 18, we see a conspicuous trend with metallicity, similar to the one shown in Sneden (1991): lower metallicity RHB and RC stars have a smaller $^{12}\text{C}/^{13}\text{C}$ range (and lower values on average) than do similar objects of higher metallicity. As discussed in, e.g. Kalirai et al. (2009) and Catelan (2009), mass loss in evolved stars increases rapidly with increasing metallicity. If the $^{12}\text{C}/^{13}\text{C}$ ratio is also related to mass-loss along with mixing processes then for a given metallicity, stars with different mass-loss and mixing history must be responsible from the $^{12}\text{C}/^{13}\text{C}$ fluctuations seen towards higher metallicities in Figure 18.

According to Charbonnel (1994), the peak of the ^{13}C abundance in the inner region of a star is shifted outward towards high initial masses. If the star evolve from high-masses ($> 2.25 M_{\odot}$), then different mechanisms, such as winds on the RGB, for mass-loss should come into play other than He-flash. Depending on how massive the star at the beginning, it might be possible for a star to dredge up some or all of its region, where the ^{13}C abundance peaks, during its RGB evolution. Since the thin disk stars are more metal-rich compared to thick disk and halo stars, the thin disk stars with higher metallicities or higher masses or a combination of both might have very low $^{12}\text{C}/^{13}\text{C}$ rates or not show any ^{13}CN feature depending on the mass fraction lost during the RGB evolution. High-mass evolving stars appear to have more options to produce a variety of surface abundances. Figure 18 should become more illuminating if we increase the number of the evolved stars which are the members of the same population. If for example we can substantially augment the RHB thick and thin disk samples, then we might have a better understanding of the mechanisms alters the CN ratios during their post-MS evolution.

We conclude by re-emphasizing our basic result: the RHB $T_{\text{eff}} - \log g$ domain of the Galactic field is populated by sub-solar metallicity thick-disk stars (as expected) but also by high metallicity thin disk stars. We will be gathering more thin and thick disk data in order to substantially increase the RHB samples of different populations to try to set additional constraints on the mechanisms that may lead to stars ending up in this relatively rare evolutionary state.

We thank Bertrand Plez for sharing his CH line lists with us, and Andy McWilliam and Inese Ivans for making their model atmosphere interpolation software available to us. MA also would like to thank The Scientific and Technological Research Council of Turkey (TÜBİTAK) for supporting her research by the “Postdoctoral Research Scholarship” program. This research has made use of NASA’s Astrophysics Data System Bibliographic Services; the SIMBAD database and the VizieR service, both operated at CDS, Strasbourg,

France; and the NASA/IPAC Extragalactic Database (NED) which is operated by the Jet Propulsion Laboratory, CalTech, under contract with NASA. Support for this study has come from the U.S. National Science Foundation grant AST 09-08978 and the Rex G. Baker, Jr. endowment to the University of Texas Department of Astronomy.

A. Appendix

HIP 46325: Super metal rich (SMR, $[\text{Fe}/\text{H}] > 0.2$) star. $[\text{Fe}/\text{H}] = 0.46$. Possible member of a moving group HR 1614 (Feltzing & Holmberg 2000). With a $V_{\text{tot}} = 64 \text{ km s}^{-1}$, probable thick disk member with high metallicity. And probable planet host (Robinson et al. 2007).

HIP 38801: $[\text{Fe}/\text{H}] = -0.06$. High-temperature star. Shows relatively high turbulence. It has peculiarly high La II and Eu II abundances. Has ^{12}C deficiency and ^{14}N enhancement, indicates a more evolved star than a SG but no $^{12}\text{C}/^{13}\text{C}$ ratio could be detected due to weak ^{13}CH or ^{13}CN features.

REFERENCES

- Alonso, A., Arribas, S., & Martínez-Roger, C. 1999, *A&AS*, 140, 261
- Allende Prieto, C., Lambert, D. L., & Asplund, M. 2001, *ApJ*, 556, L63
- Anthony-Twarog, B. J., Atwell, J., & Twarog, B. A. 2005, *AJ*, 129, 872
- Aoki, W., Honda, S., Beers, T. C., & Sneden, C. 2003a, *ApJ*, 586, 506
- Aoki, W., et al. 2003b, *ApJ*, 592, L67
- Asplund, M., Grevesse, N., Sauval, A. J., & Scott, P. 2009, *ARA&A*, 47, 481
- Aurière, M. 1982, *A&A*, 109, 301
- Bensby, T. & Feltzing, S., 2010, in *Chemical Abundances in the Universe: Connecting First Stars to Planets*, Proc. IAU Symp. 265, 300
- Bensby, T., Feltzing, S., & Lundström, I. 2004, *A&A*, 415, 155
- Bensby, T., Feltzing, S., & Lundström, I. 2003, *A&A*, 410, 527
- Bertelli, G., Girardi, L., Marigo, P. & Nasi, E. 2008, *A&A*, 484, 815

- Boothroyd, A. I., Sackmann, I. J. 1999, ApJ, 510, 232
- Canizares, C. R., Grindlay, J. E., Hiltner, W. A., Liller, W., & McClintock, J. E. 1978, ApJ, 224, 39
- Cannon, R. D. 1970, MNRAS, 150, 111
- Castelli, F., Gratton, R. G., & Kurucz, R. L. 1997, A&A, 318, 841
- Castelli, F., & Kurucz, R. L. 2003, Modelling of Stellar Atmospheres, IAU Symposium 210, 20P
- Catelan, M. 2009, IAU Symposium, 258, 209
- Cenarro, A. J., et al. 2007, MNRAS, 374, 664
- Charbonnel, C. 1994, A&A, 282, 811
- Charbonnel, C., Brown, J. A., & Wallerstein, G. 1998, A&A, 332, 204
- Charbonnel, C., & Balachandran, S. C. 2000, A&A, 359, 563
- Charbonnel, C., & Zahn, J.-P. , A&A, 467, L15
- Charbonnel, C., & Lagarde, N. 2010, A&A, 522, 10
- Chen, Y. Q., Nissen, P. E., Zhao, G., Zhang, H. W., & Benoni, T. 2000, A&AS, 141, 491
- Chen, B., Vergely, J. L., Valette, B., & Carraro, G. 1998, A&A, 336, 137
- Cottrell, P. L., & Sneden, C. 1986, A&A, 161, 314
- Dinescu, D. I., Girard, T. M., & van Altena, W. F. 1999, AJ, 117, 1792
- Dehnen, W., & Binney, J. J. 1998, MNRAS, 298, 387
- Feltzing, S., & Holmberg, J. 2000, A&A, 357, 153
- Delbouille, L., Roland, G., & Neven, L. 1973, Atlas photometrique du spectre solaire de $\lambda 3000$ a $\lambda 10000$, Liege: Universite de Liege, Institut d’Astrophysique
- Fitzpatrick, M. J., 1993, in Astronomical Data Analysis Software and Systems II, ed. R. J. Hanisch, R. V. J. Brissenden, & J. Barnes (San Francisco: ASP), ASP Conf. Ser., 52, 472
- Fitzpatrick, M. J., & Sneden, C. 1987, BAAS, 19, 1129

- Franchini, M., Morossi, C., Di Marcantonio, P., Malagnini, M. L., Chavez, M., & Rodríguez-Merino, L. 2004, *ApJ*, 613, 312
- Gilmore, G., & Reid, N. 1983, *MNRAS*, 202, 1025
- Gratton, R. G., Carretta, E., Eriksson, K., & Gustafsson, B. 1999, *A&A*, 350, 955
- Gratton, R. G., Sneden, C., Carretta, E., & Bragaglia, A. 2000, *A&A*, 354, 169
- Gray, D. F., & Brown, K. 2001, *PASP*, 113, 723
- Gray, R. O., & Corbally, C. J. 2009, *Stellar Spectral Classification*, (Princeton: Princeton University Press)
- Grenon, M. 1972, *IAU Colloq. 17: Age des Etoiles*, 29
- Grevesse, N., & Sauval, A. J. 1998, *Space Sci. Rev.*, 85, 161
- Griffin, R. 1968, *A Photometric Atlas of the Spectrum of Arcturus, $\lambda\lambda$ 3600–8825 Å*, Cambridge: Cambridge Philosophical Society
- Hakkila, J., Myers, J. M., Stidham, B. J., & Hartmann, D. H. 1997, *AJ*, 114, 2043
- Harlan, E. A. 1969, *AJ*, 74, 916
- Harlan, E. A. 1974, *AJ*, 79, 682
- Harlan, E. A. 1981, *AJ*, 86, 1896
- Henry, G. W., Fekel, F. C., Henry, S. M., & Hall, D. S. 2000, *ApJS*, 130, 201
- Hesser, J. E., Harris, W. E., Vandenberg, D. A., Allwright, J. W. B., Shott, P., & Stetson, P. B. 1987, *PASP*, 99, 739
- Hill, V., et al. 2002, *A&A*, 387, 560
- Hollek, J. K., Frebel, A., Roederer, I. U., Sneden, C., Shetrone, M., Beers, T. C., Kang, S.-J., & Thom, C. 2011, *ApJ*, in press
- Iben, I. Jr. 1964, *ApJ*, 140, 1631
- Iben, I. Jr. 1965, *ApJ*, 142, 1447
- Iben, I., Jr. 1967a, *ApJ*, 147, 624
- Iben, I. Jr. 1967b, *ApJ*, 147, 650

- Ivans, I. I., Simmerer, J., Sneden, C., Lawler, J. E., Cowan, J. J., Gallino, R., & Bisterzo, S. 2006, *ApJ*, 645, 613
- Jacobson, H. R., Friel, E. D., & Pilachowski, C. A. 2011, *AJ*, 141, 58
- Johansson, S., Litzén, U., Lundberg, H., & Zhang, Z. 2003, *ApJ*, 584, L107
- Johnson, D. R. H., & Soderblom, D. R. 1987, *AJ*, 93, 864
- Kaempf, T. A., de Boer, K. S., & Altmann, M. 2005, *A&A*, 432, 879
- Kalirai, J. S., Saul Davis, D., Richer, H. B., et al. 2009, *ApJ*, 705, 408
- Kjaergaard, P., Gustafsson, B., Walker, G. A. H., & Hultqvist, L. 1982, *A&A*, 115, 145
- Kumar, Y. B., Reddy, B. E., & Lambert, D. L. 2011, *ApJ*, 730, L12
- Kurucz, R. L. 2011, *Canadian Journal of Physics*, 89, 417
- Lallement, R., Welsh, B. Y., Vergely, J. L., Crifo, F., & Sfeir, D. 2003, *A&A*, 411, 447
- Lambert, D. L., & Ries, L. M. 1981, *ApJ*, 248, 228
- Lawler, J. E., Bonvallet, G., & Sneden, C. 2001a, *ApJ*, 556, 452
- Lawler, J. E., Wickliffe, M. E., den Hartog, E. A., & Sneden, C. 2001b, *ApJ*, 563, 1075
- Lee, Y. S., Beers, T. C., An, D., et al. 2011, *ApJ*, 738, 187
- Lee, Y.-W., Demarque, P., & Zinn, R. 1994, *ApJ*, 423, 248
- Liu, Y., Sato, B., Takeda, Y., Ando, H., & Zhao, G. 2010, *PASJ*, 62, 1071
- Luck, R. E., & Heiter, U. 2007, *AJ*, 133, 2464
- Mallik, S. V. 1998, *A&A*, 338, 623
- Mashonkina, L., Gehren, T., Shi, J.-R., Korn, A. J., & Grupp, F. 2011, *A&A*, 528, A87
- McWilliam, A. 1990, *ApJS*, 74, 1075
- Mishenina, T. V., Bienaymé, O., Gorbaneva, T. I., Charbonnel, C., Soubiran, C., Korotin, S. A., & Kovtyukh, V. V. 2006, *A&A*, 456, 1109
- Mishenina, T. V., Gorbaneva, T. I., Bienaymé, O., et al. 2007, *Astronomy Reports*, 51, 382
- Monaco, L., Villanova, S., Moni Bidin, C., Carraro, G., et al. 2011, 529, A90

- Moore, C. E., Minnaert, M. G. J., & Houtgast, J. 1966, The solar spectrum 2935 Å to 8770 Å, Nat. Bur. Stds. Monograph, Washington: US Government Printing Office
- Nissen, P. E., 2004, in Origin and Evolution of the Elements, Carnegie Observatories Astrophysics Series, Vol. 4, (Eds.) A. McWilliam and M. Rauch, Pasadena: Carnegie Observatories, p. 154
- Nordström, B., et al. 2004, A&A, 418, 989
- Norris, J. 1987, AJ, 93, 616
- Omiya, M., et al. 2009, PASJ, 61, 825
- Perryman, M. A. C., et al. 1997, A&A, 323, L49
- Piersanti, L., Tornambé, A., & Castellani, V. 2004, MNRAS, 353, 243
- Plez, B., & Cohen, J. G. 2005, A&A, 434, 1117
- Ralchenko, Yu., Kramida, A.E., Reader, J., and NIST ASD Team 2011, NIST Atomic Spectra Database (ver. 4.1.0), National Institute of Standards and Technology, Gaithersburg, MD
- Ramírez, I., & Meléndez, J. 2005, ApJ, 626, 465
- Reddy, B. E., Lambert, D. L., & Allende Prieto, C. 2006, MNRAS, 367, 1329
- Reddy, B. E., Tomkin, J., Lambert, D. L., & Allende Prieto, C. 2003, MNRAS, 340, 304
- Robinson, S. E., Ammons, S. M., Kretke, K. A., Strader, J., Wertheimer, J. G., Fischer, D. A., & Laughlin, G. 2007, ApJS, 169, 430
- Roederer, I. U., Lawler, J. E., Sneden, C., et al. 2008, ApJ, 675, 723
- Rose, J. A. 1985, AJ, 90, 787
- Rosenberg, A., Piotto, G., Saviane, I., Aparicio, A. 2000a, A&AS, 144, 5
- Rosenberg, A., Aparicio, A., Saviane, I., & Piotto, G. 2000b, A&AS, 145, 451
- Ryan, S. G., & Lambert, D. L. 1995, AJ, 109, 2068
- Sandage, A. 1972, ApJ, 178, 1
- Schaller, G., Schaerer, D., Meynet, G., & Maeder, A. 1992, A&AS, 96, 269

- Simmerer, J., Sneden, C., Cowan, J. J., Collier, J., Woolf, V. M., & Lawler, J. E. 2004, *ApJ*, 617, 1091
- Smith, V. V., Lambert, D. L., & Nissen, P. E. 1998, *ApJ*, 506, 405
- Sneden, C. 1973, *ApJ*, 184, 839
- Sneden, C. 1991, *Evolution of Stars: the Photospheric Abundance Connection*, 145, 235
- Sneden, C., Cowan, J. J., & Gallino, R. 2008, *ARA&A*, 46, 241
- Sneden, C., Cowan, J. J., Lawler, J. E., et al. 2002, *ApJ*, 566, L25
- Sneden, C., Pilachowski, C. A., & Vandenberg, D. A. 1986, *ApJ*, 311, 826
- Soubiran, C., & Girard, P. 2005, *A&A*, 438, 139
- Soubiran, C., Bienaymé, O., Mishenina, T. V., & Kovtyukh, V. V. 2008, *A&A*, 480, 91
- Stetson, P. B., & Aikman, C. L. 1987, *AJ*, 93, 1439
- Straižys, V., Bartkevicius, A., & Sperauskas, J. 1981, *A&A*, 99, 152
- Strassmeier, K. G., & Schordan, P. 2000, *Astronomische Nachrichten*, 321, 277
- Sweigart, A. V., & Gross, P. G. 1978, *ApJS*, 36, 405
- Takeda, Y., Sato, B., Kambe, E., et al. 2005, *PASJ*, 57, 109
- Takeda, Y., Sato, B., & Murata, D. 2008, *PASJ*, 60, 781
- Tautvaišienė, G. 1996, *Astronomische Nachrichten*, 317, 29
- Tautvaišienė, G. 1997, *MNRAS*, 286, 948
- Tautvaišienė, G., Edvardsson, B., Tuominen, I., & Ilyin, I. 2001, *A&A*, 380, 578
- Thorén, P., Edvardsson, B., & Gustafsson, B. 2004, *A&A*, 425, 187
- Tull, R. G., MacQueen, P. J., Sneden, C., & Lambert, D. L. 1995, *PASP*, 107, 251
- Ungren, A. R. 1962, *AJ*, 67, 37
- Ungren, A. R. 1963, *AJ*, 68, 194
- van Leeuwen, F. 2007, *A&A*, 474, 653

Venn, K. A., Irwin, M., Shetrone, M. D., et al. 2004, *AJ*, 128, 1177

Wilson, O. C. 1976, *ApJ*, 205, 823

Zahn, J.-P. 1992, *A&A*, 265, 115

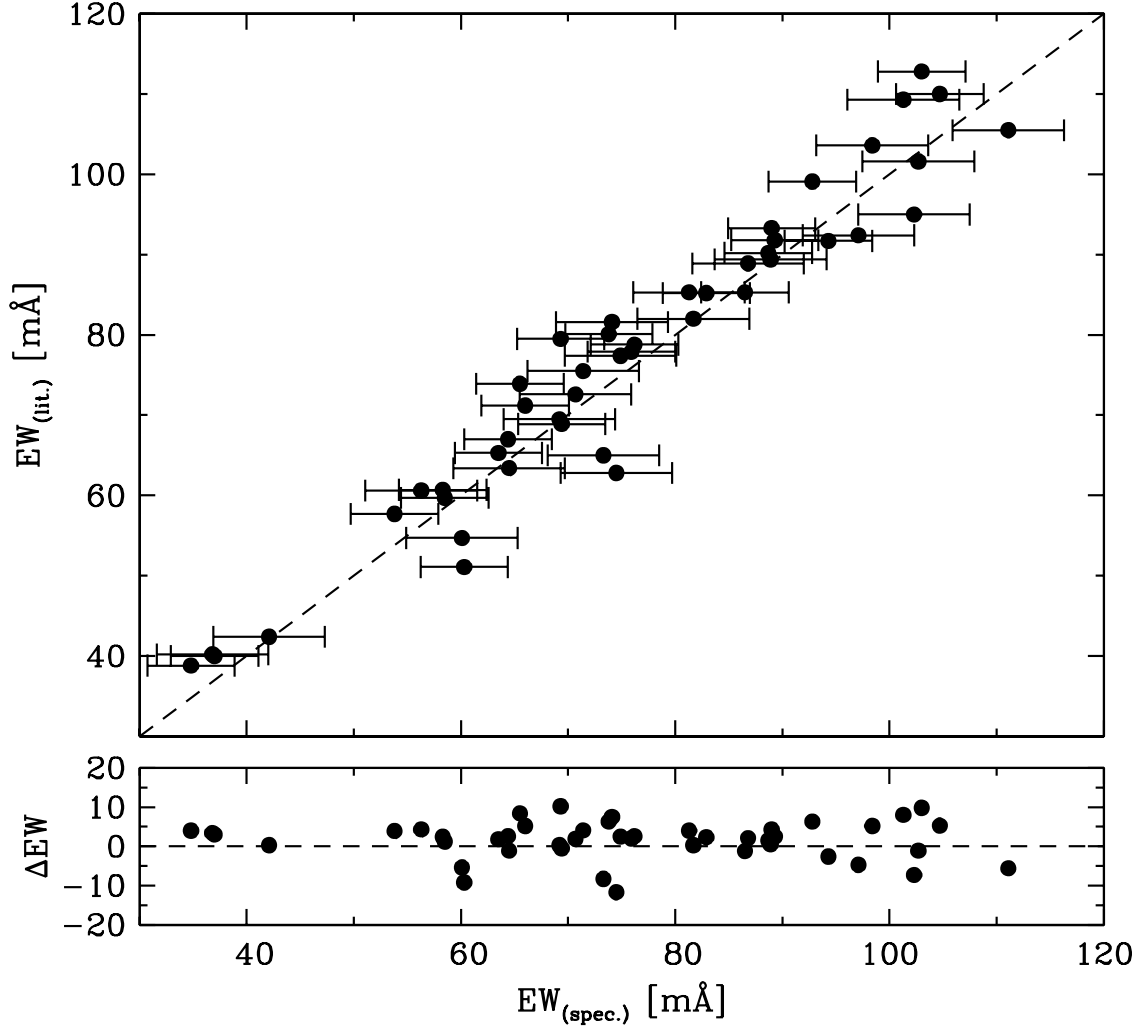


Fig. 1.— Top panel: comparison of our EWs with previous studies for HIP 13339 and HIP 71837 (Takeda et al. 2005). Bottom panel: differences in EWs, defined as $\Delta EW \equiv EW_{\text{literature}} - EW_{\text{thisstudy}}$. Error bars represent the $\sigma \simeq 5 \text{ m}\text{\AA}$ of ΔEW .

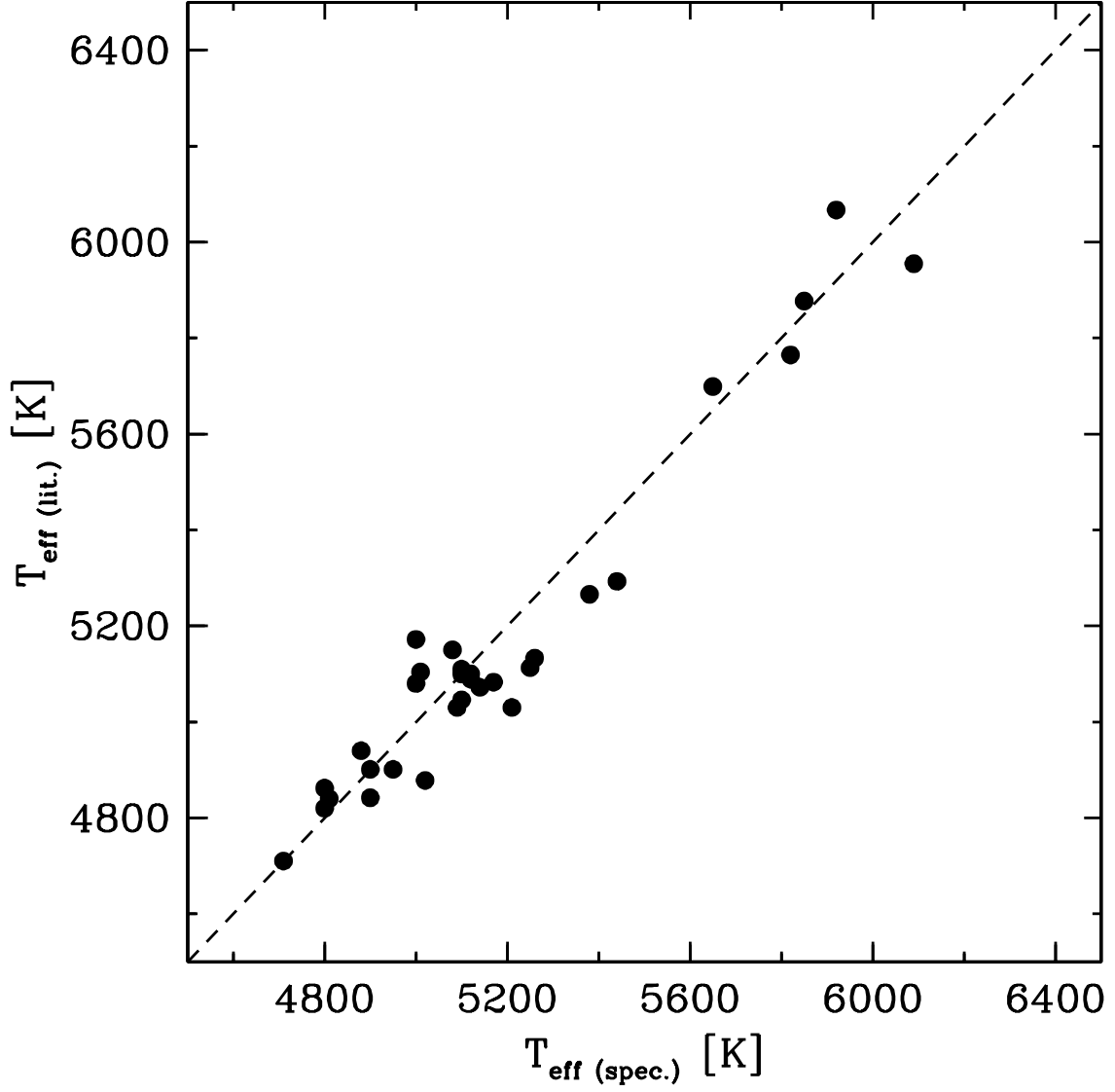


Fig. 2.— Comparison of our derived spectroscopic T_{eff} values with those gathered from heterogeneous literature (filled circles): Cottrell & Sneden (1986), McWilliam (1990), Ryan & Lambert (1995), Mallik (1998), Chen et al. (2000), Tautvaišienė et al. (2001), Franchini et al. (2004), Nordström et al. (2004), Luck & Heiter (2007), Robinson et al. (2007), Soubiran et al. (2008), Takeda et al. (2008), Omiya et al. (2009), and Liu et al. (2010).

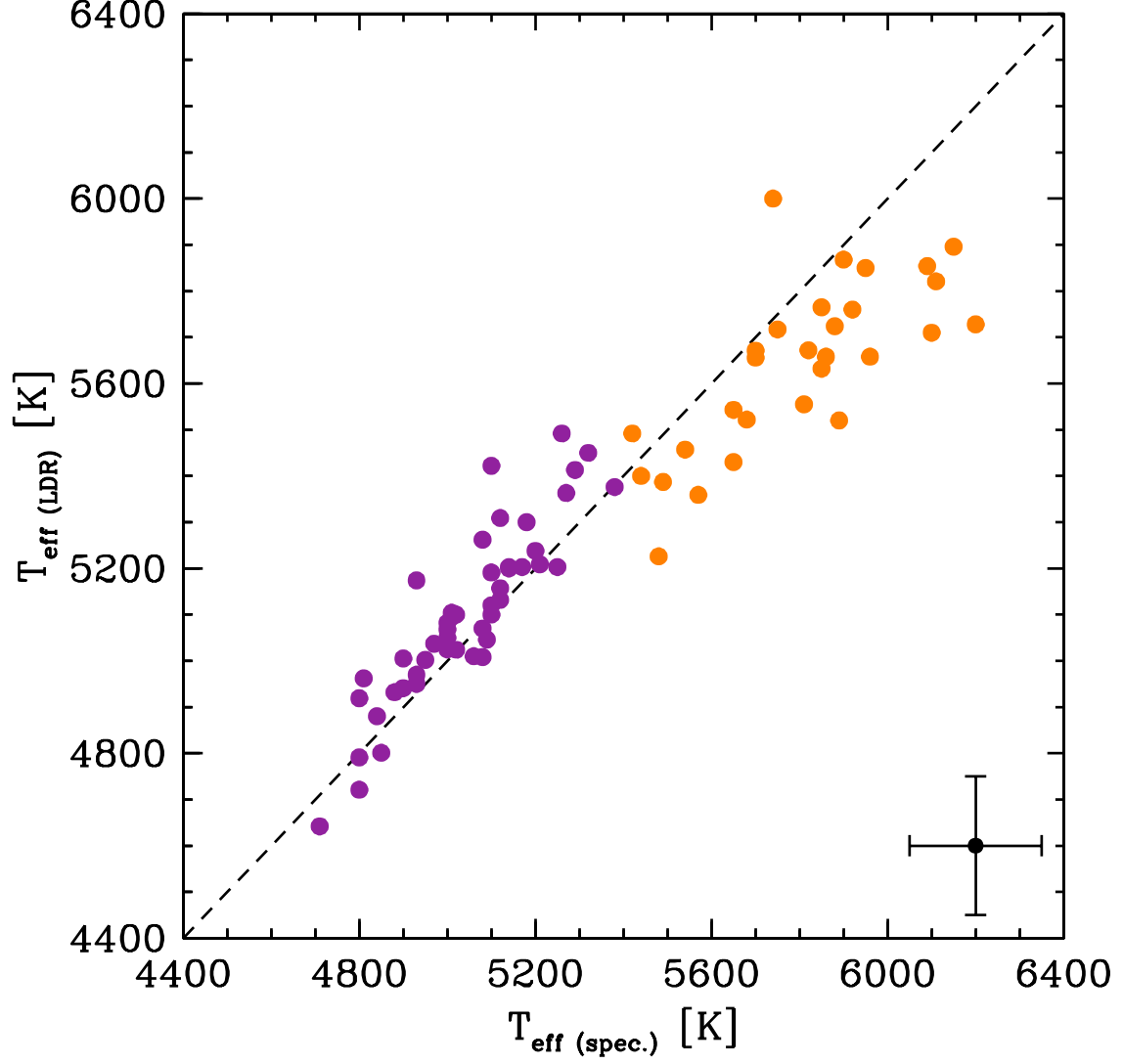


Fig. 3.— Comparison of our spectroscopic T_{eff} with the ones obtained using LDR method. A break in the relation is seen at $T_{\text{eff}} < 5500 \text{ K}$, which we call attention to by using different symbol colors for stars warmer and cooler than this temperature; see text for discussion of this issue.

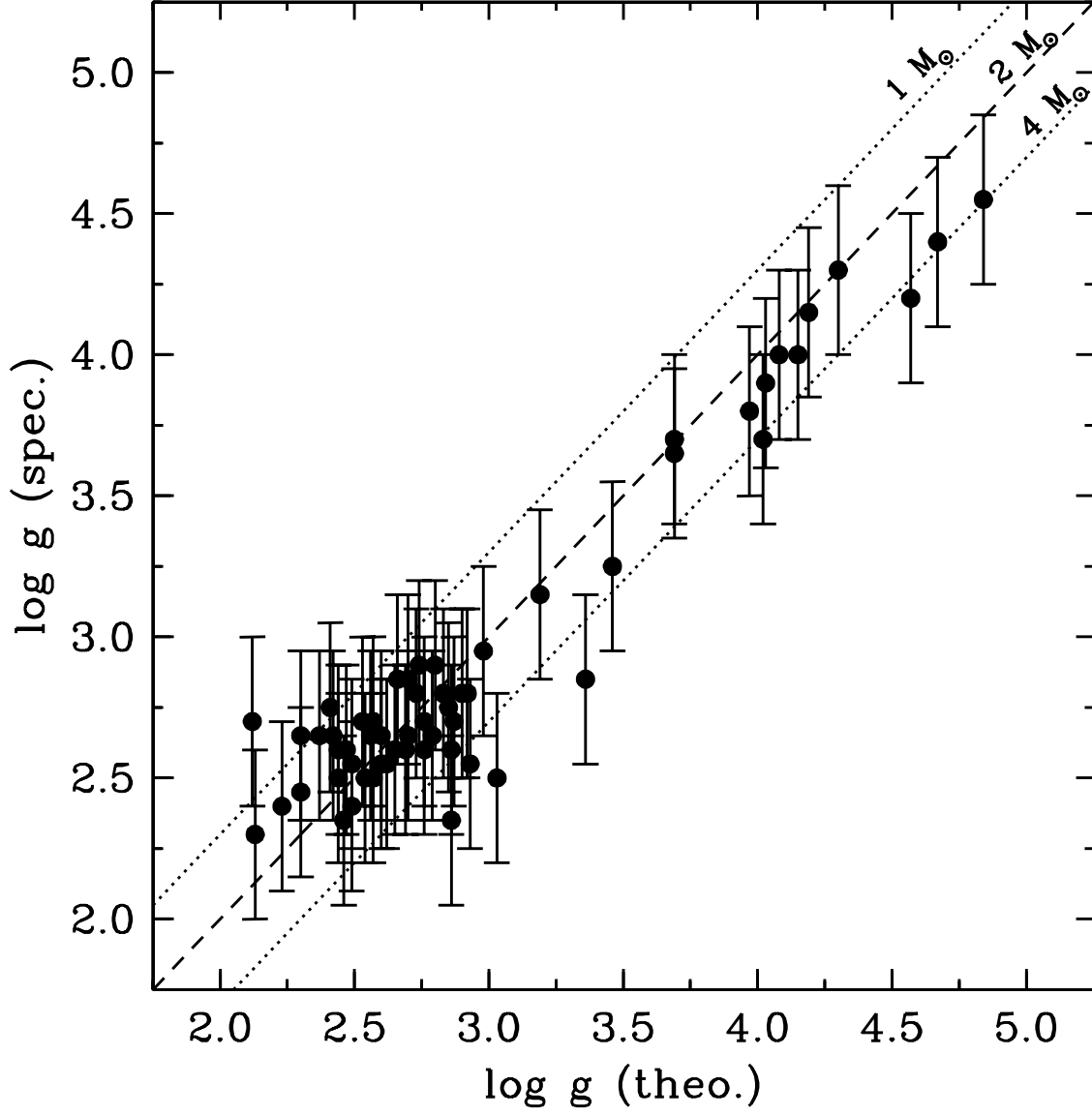


Fig. 4.— Comparison of our spectroscopic $\log g$ values with theoretical ones. $\log g(\text{theo.})$ are calculated for $M = 1, 2$ and $4 M_{\odot}$ (dashed and dotted lines). The uncertainty for our spectral $\log g$ is ± 0.3 dex. We do not have errors on the theoretical values since those are adopted masses.

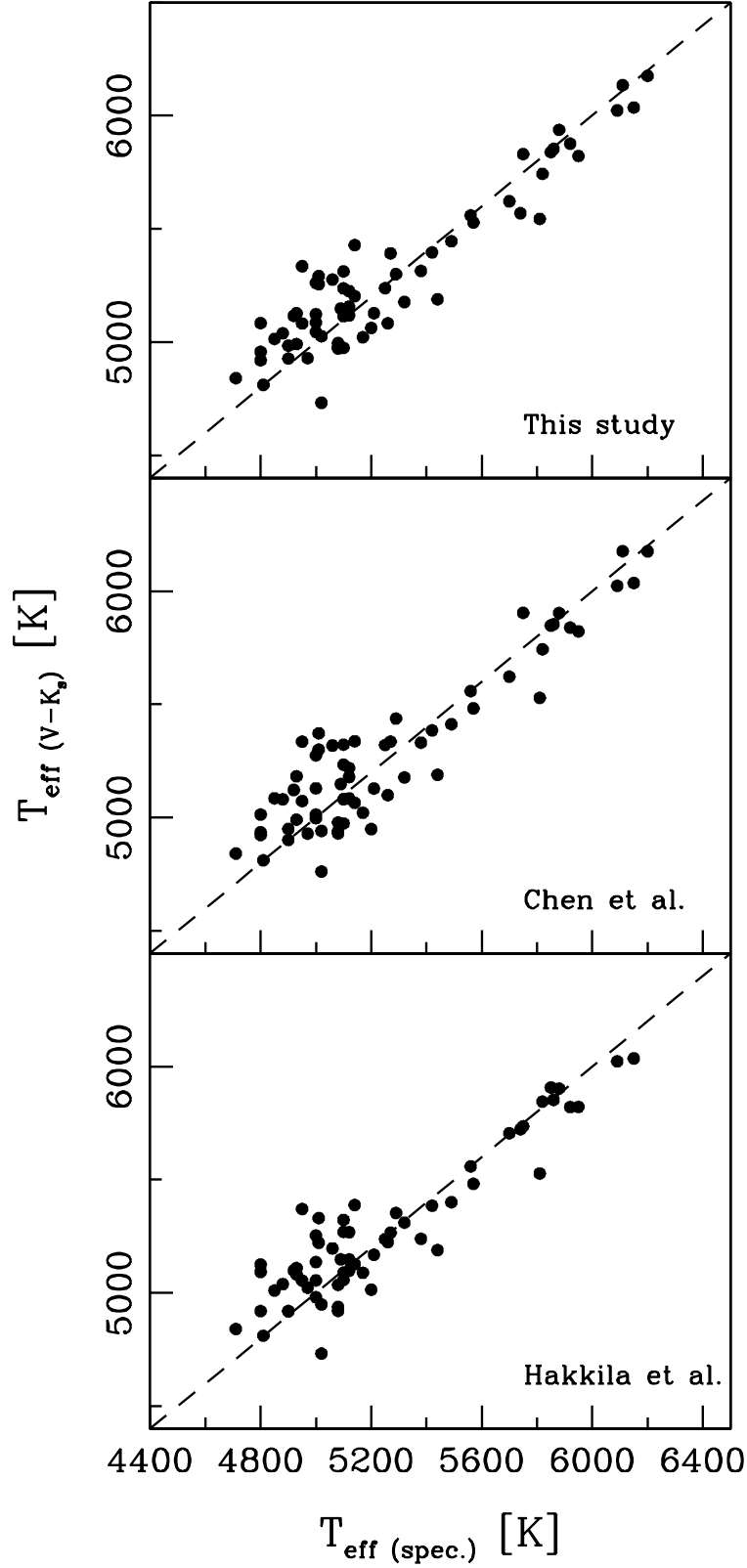


Fig. 5.— Comparison of spectroscopic $T_{\text{eff (spec.)}$ with photometric $T_{\text{eff (V-K}_s\text{)}}$, adopting the three different reddening estimates discussed in §3.2.

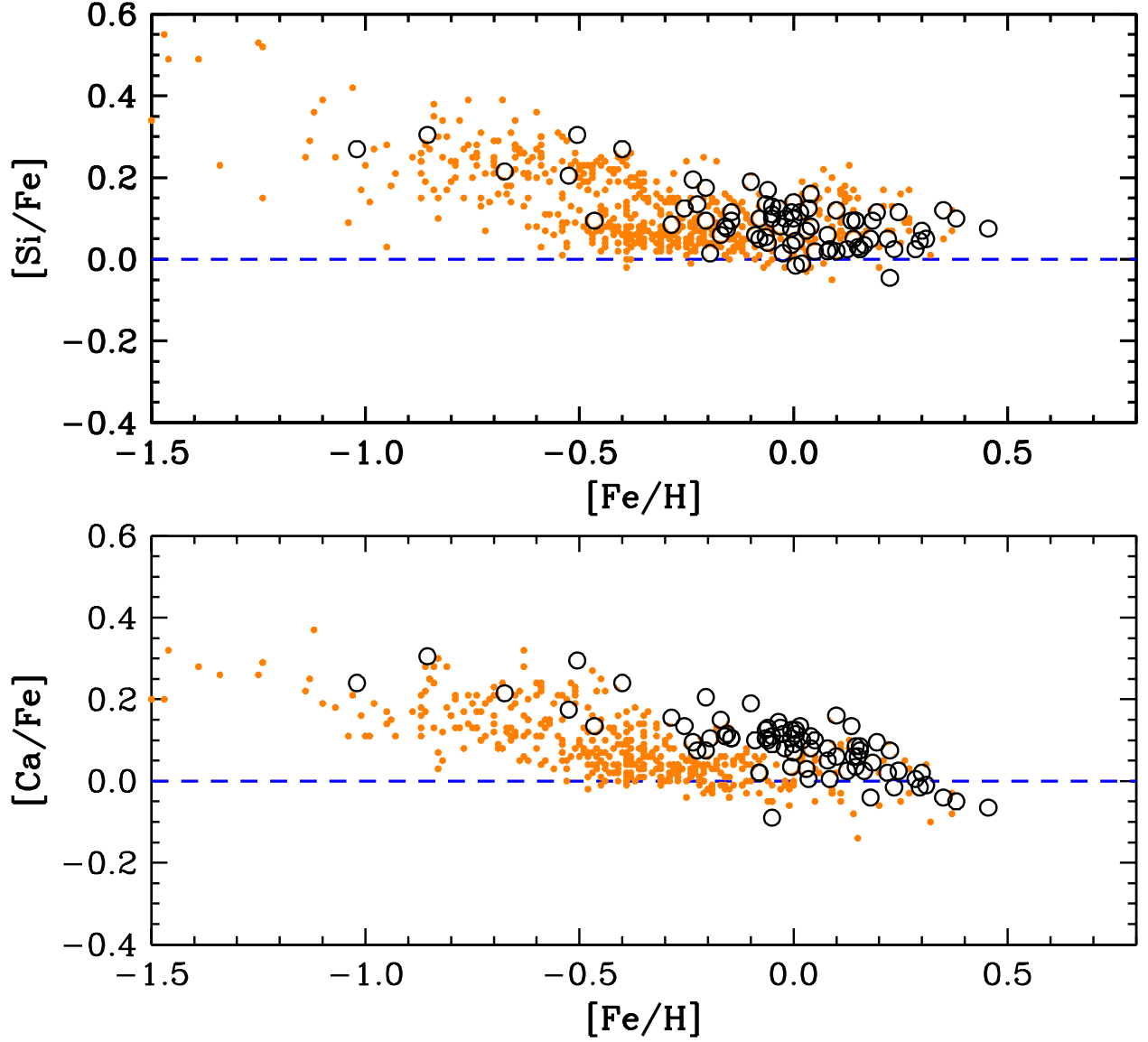


Fig. 6.— Relative Si and Ca abundances in our program stars (black open circles) and in stars in the literature (orange dots). All results are based on lines of Si I and Ca I species. The data from the literature are adopted without adjustment from Tautvaišienė et al. (2001), Bensby et al. (2003), Reddy et al. (2003, 2006) and Mishenina et al. (2006).

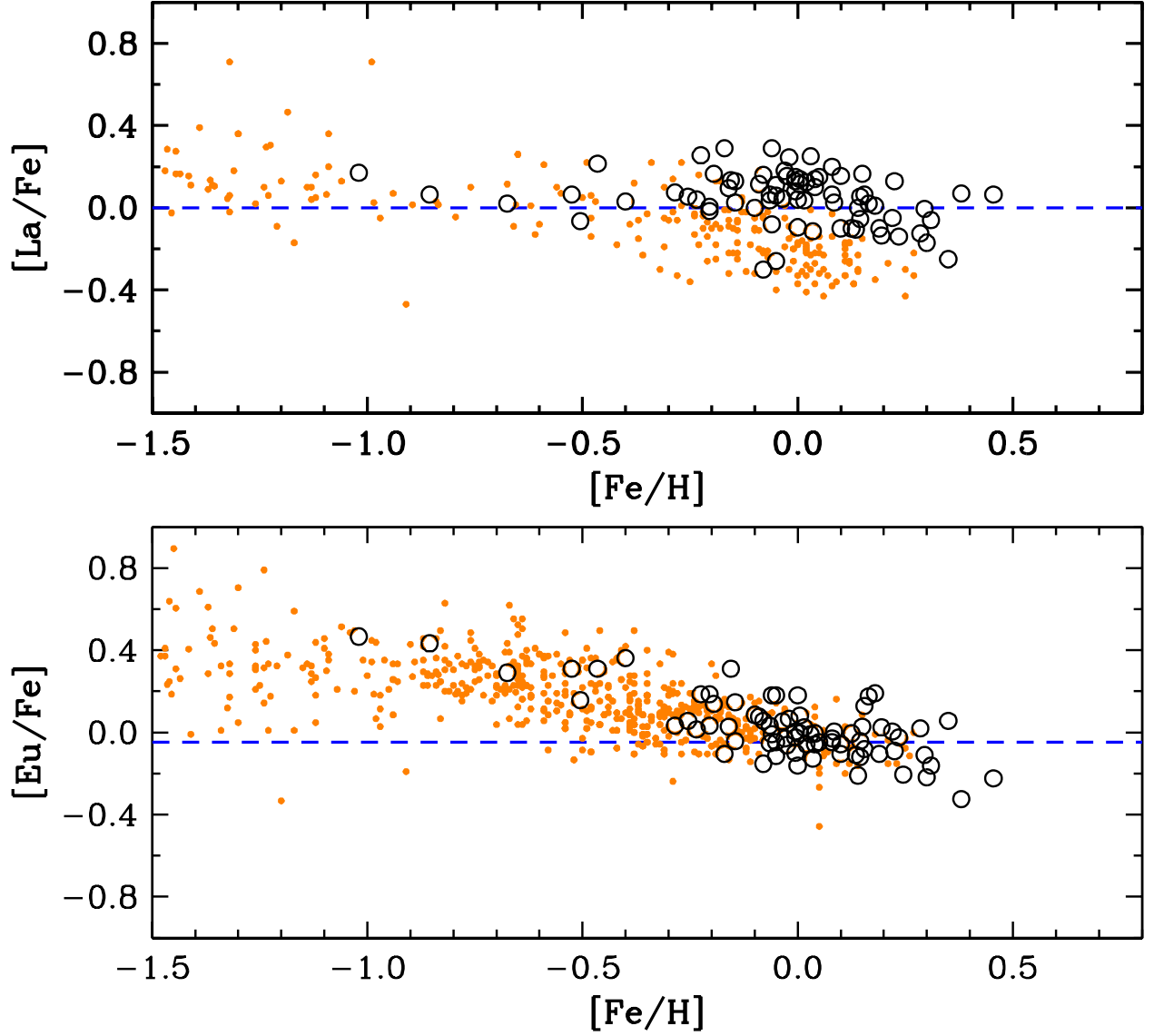


Fig. 7.— Relative La and Eu abundances in our program stars (black open circles) and in stars in the literature (orange dots). All results are based on lines of La II and Eu II species. The data from the literature are adopted without adjustment from Tautvaišienė et al. (2001), Bensby et al. (2003), Venn et al. (2004), Simmerer et al. (2004), Reddy et al. (2003, 2006) and Mishenina et al. (2007).

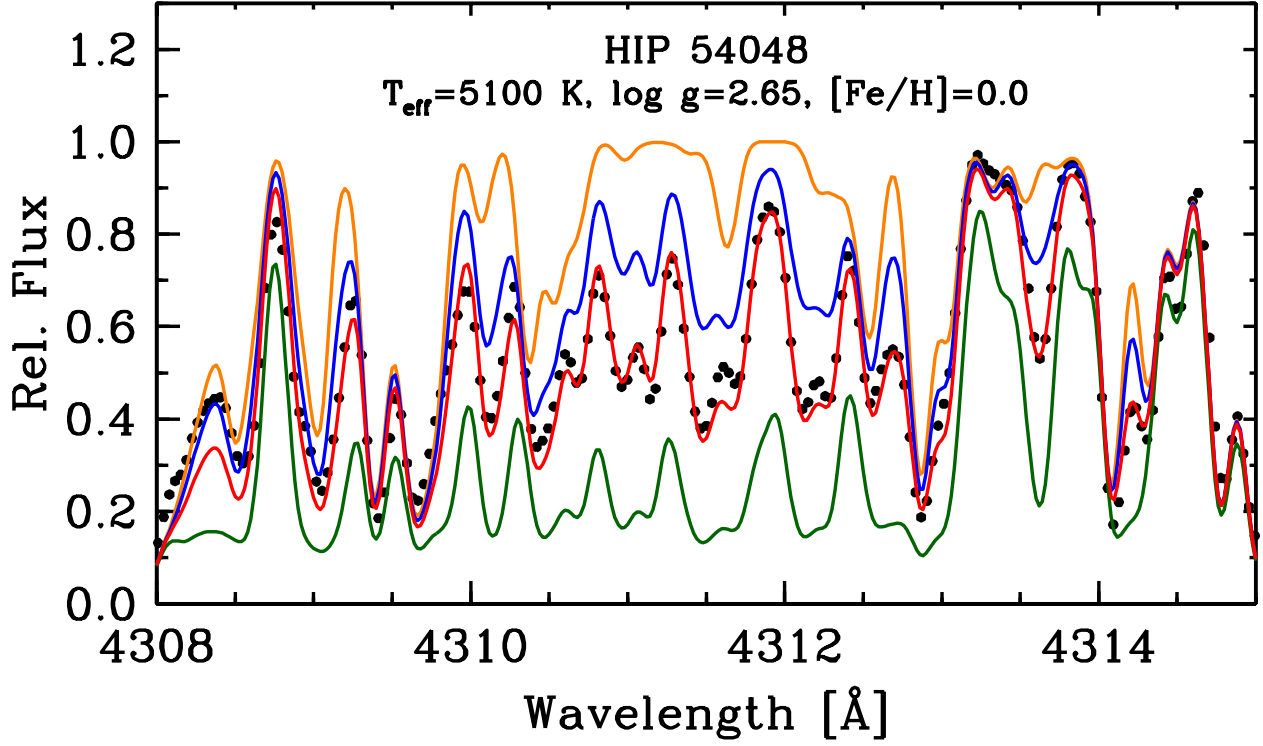


Fig. 8.— Comparison of synthetic and observed spectrum of HIP 54048 for a part of the CH G-band region. Best fit is illustrated by a red solid line for $\log \epsilon(\text{C})=7.79$. Other fits represented by yellow, blue and green solid lines are given for $\log \epsilon(\text{C})=2.79$, 7.34 and 8.69, respectively.

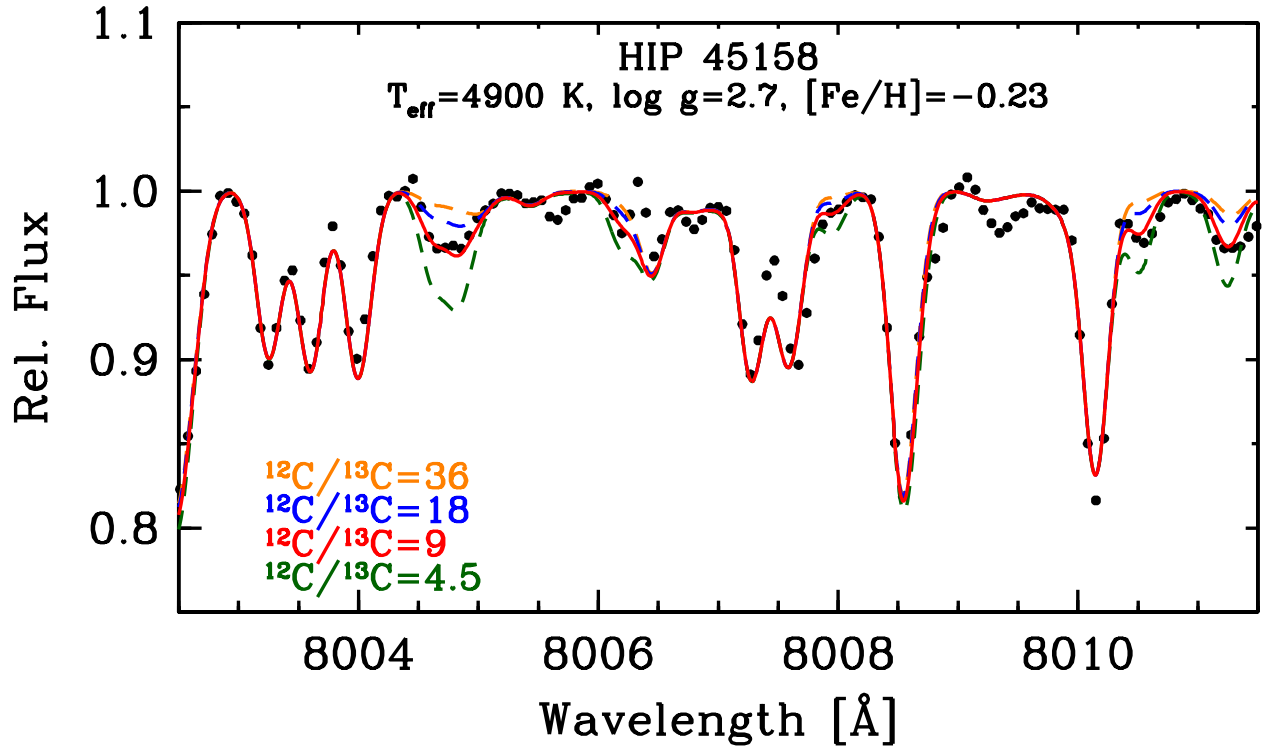


Fig. 9.— Comparison of synthetic and observed spectrum of HIP 45158 for observed ^{13}CN feature around 8004 \AA . Best fit is illustrated by a red solid line for $^{12}\text{C}/^{13}\text{C} = 9$. Other trials are also shown for $^{12}\text{C}/^{13}\text{C}$ values of 36, 18 and 4.5 (dashed lines).

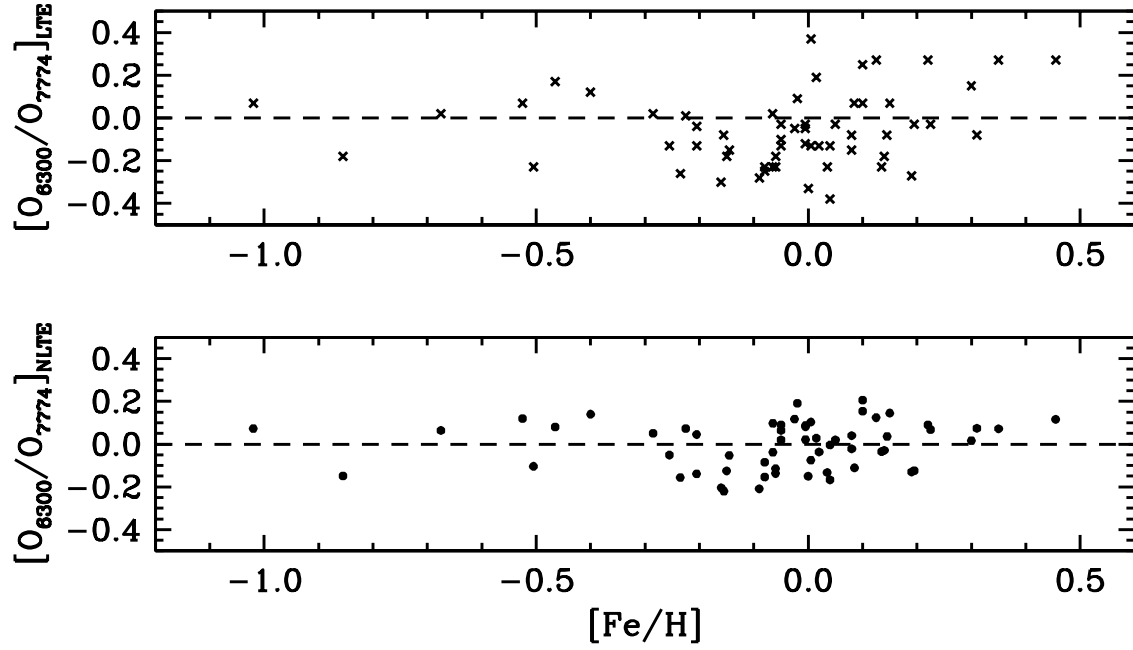


Fig. 10.— Application of NLTE correction to the O I triplet. Upper panel (crosses) shows before, bottom panel (dots) shows after the correction applied.

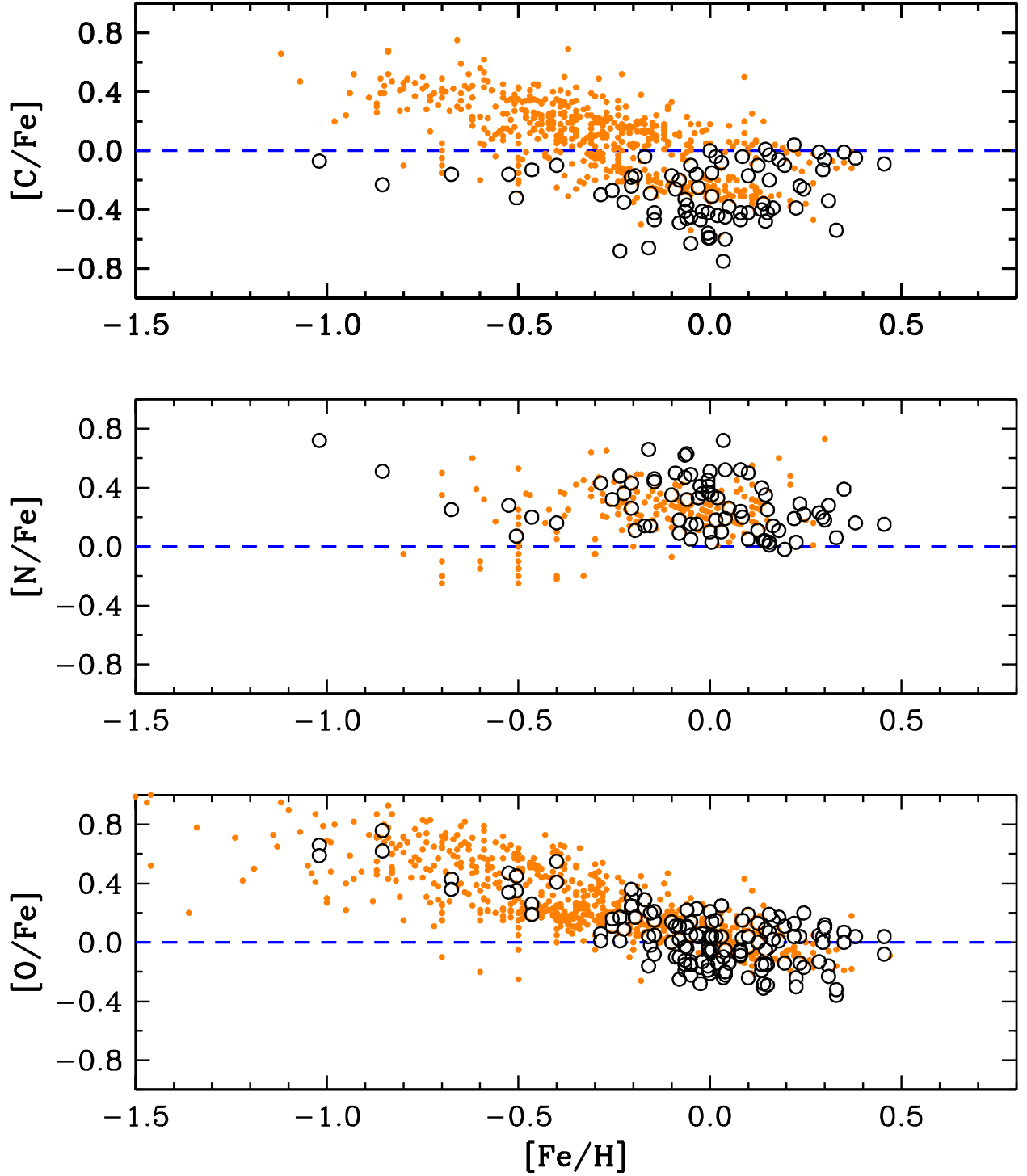


Fig. 11.— Relative C, N and O abundances in our program stars (black open circles) and in stars in the literature (orange dots). All results are based on lines of C I_{CH}, N I from CN8020 Å region and O I₆₃₀₀ as well as NLTE-corrected O I from 7774 triplets species. The data from the literature are adopted without adjustment from Lambert & Ries (1981), Cottrell & Sneden (1986), Tautvaišienė et al. (2001), Bensby et al. (2003), Reddy et al. (2003, 2006) and Mishenina et al. (2006).

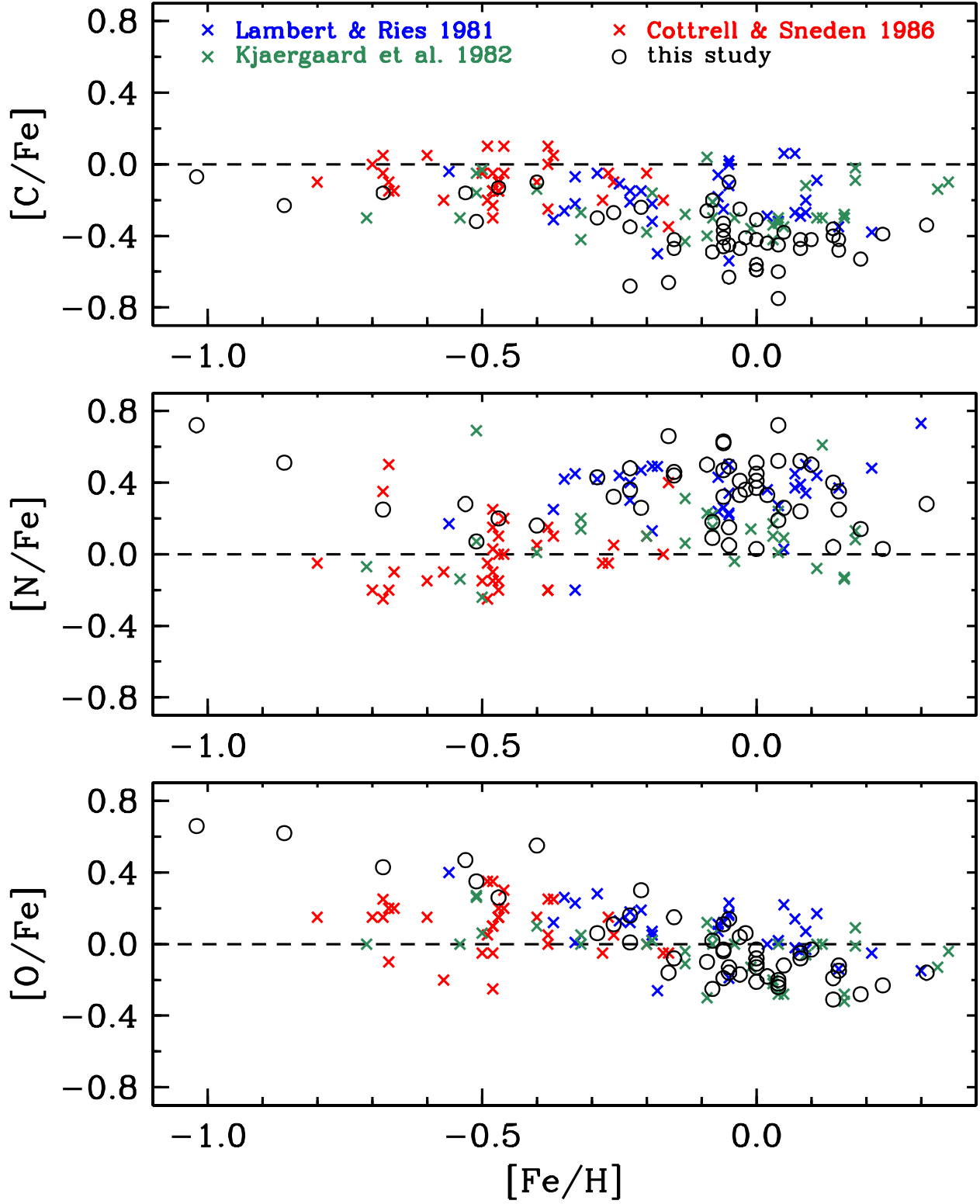


Fig. 12.— The C, N and O abundances in our program stars (open circles) and in samples of evolved (red giant) stars in the literature (crosses). Different colors have been used to denote results from other studies, according to the legend given in the top panel.

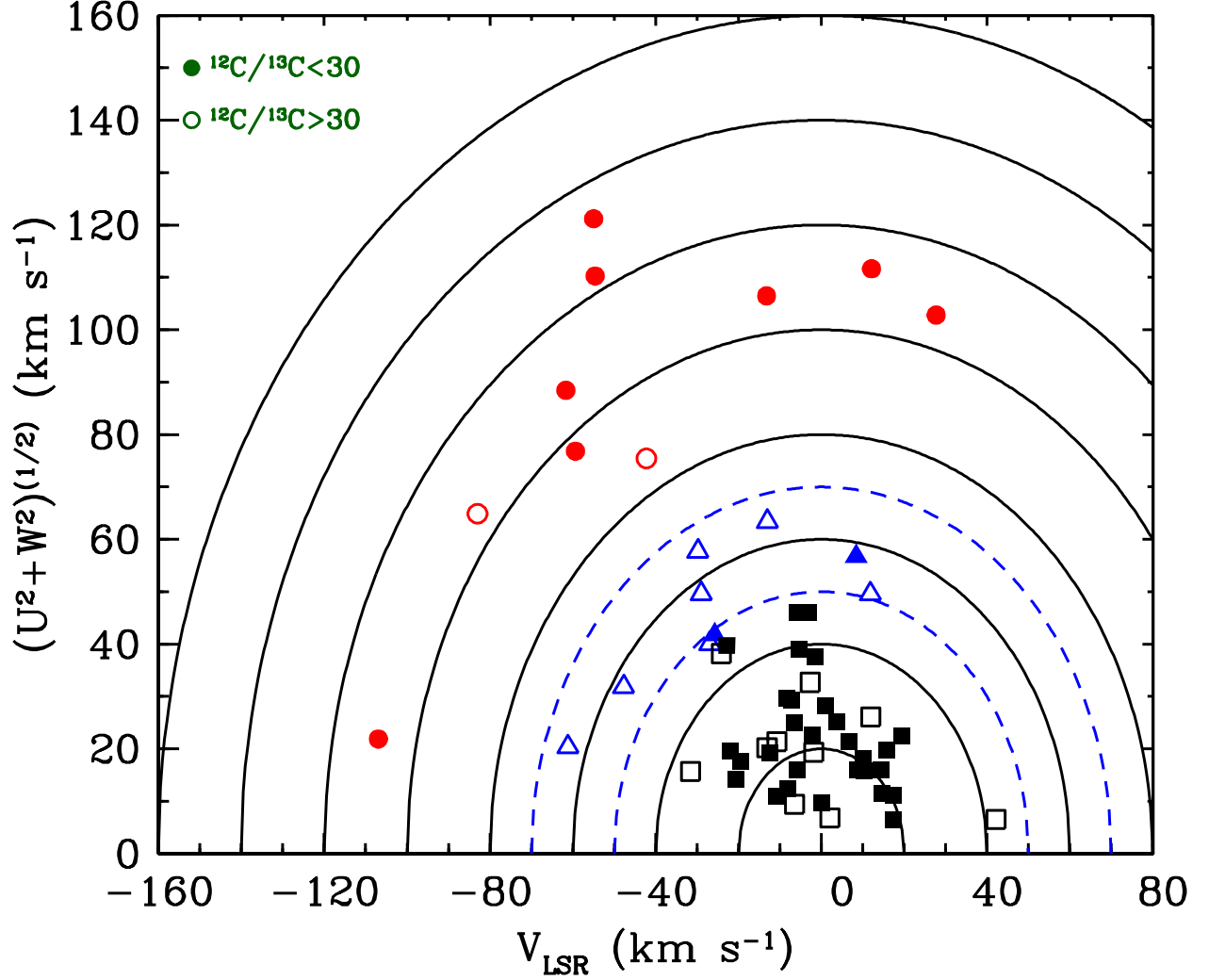


Fig. 13.— Toomre diagram of the program stars. Solid lines indicate V_{tot} in steps of 20 km s⁻¹. The dashed lines at 50 and 70 km s⁻¹ denotes the approximate thin-thick disk separation. Thin, thin/thick and thick disk stars are represented by (black) squares, (blue) triangles and (red) circles. Filled and open symbols represent whether $^{12}\text{C}/^{13}\text{C}$ is detected in the spectrum of the related star (representative filled and open symbols and their meaning are also shown in the figure).

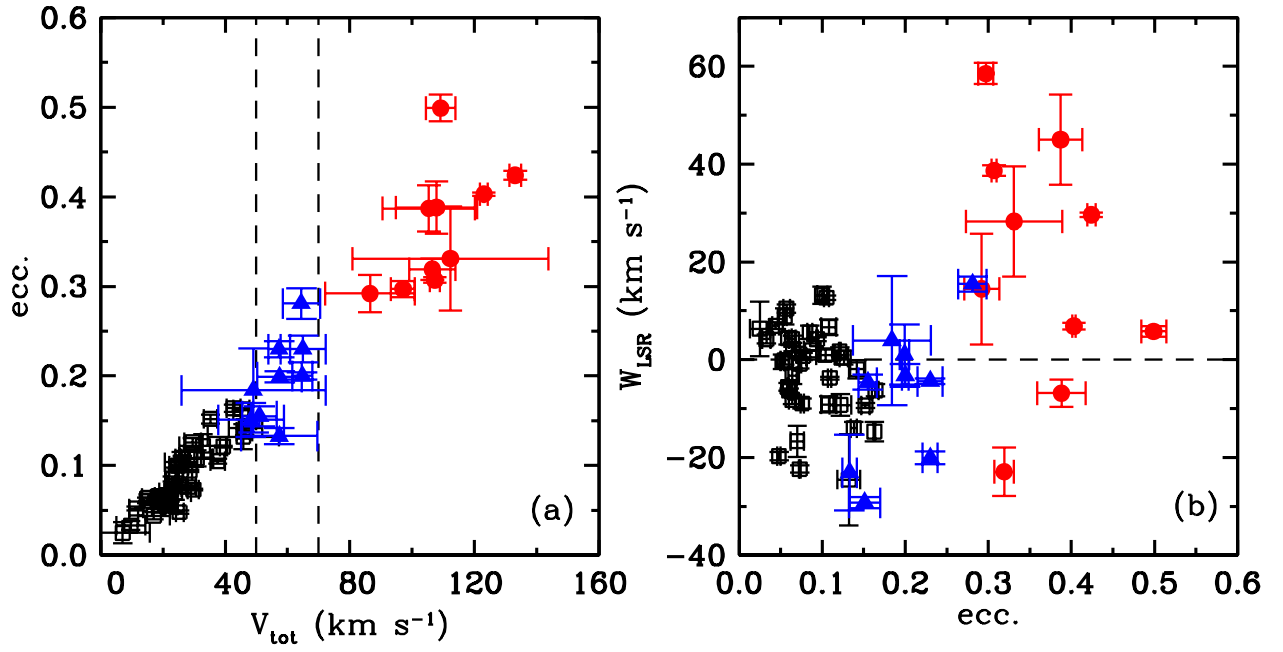


Fig. 14.— Panel (a): correlation of Galactic orbital eccentricity $ecc.$ with total space velocity V_{tot} . Panel (b): correlation of vertical velocity component W_{LSR} with eccentricity. The symbol colors are the same as those of Figure 13.

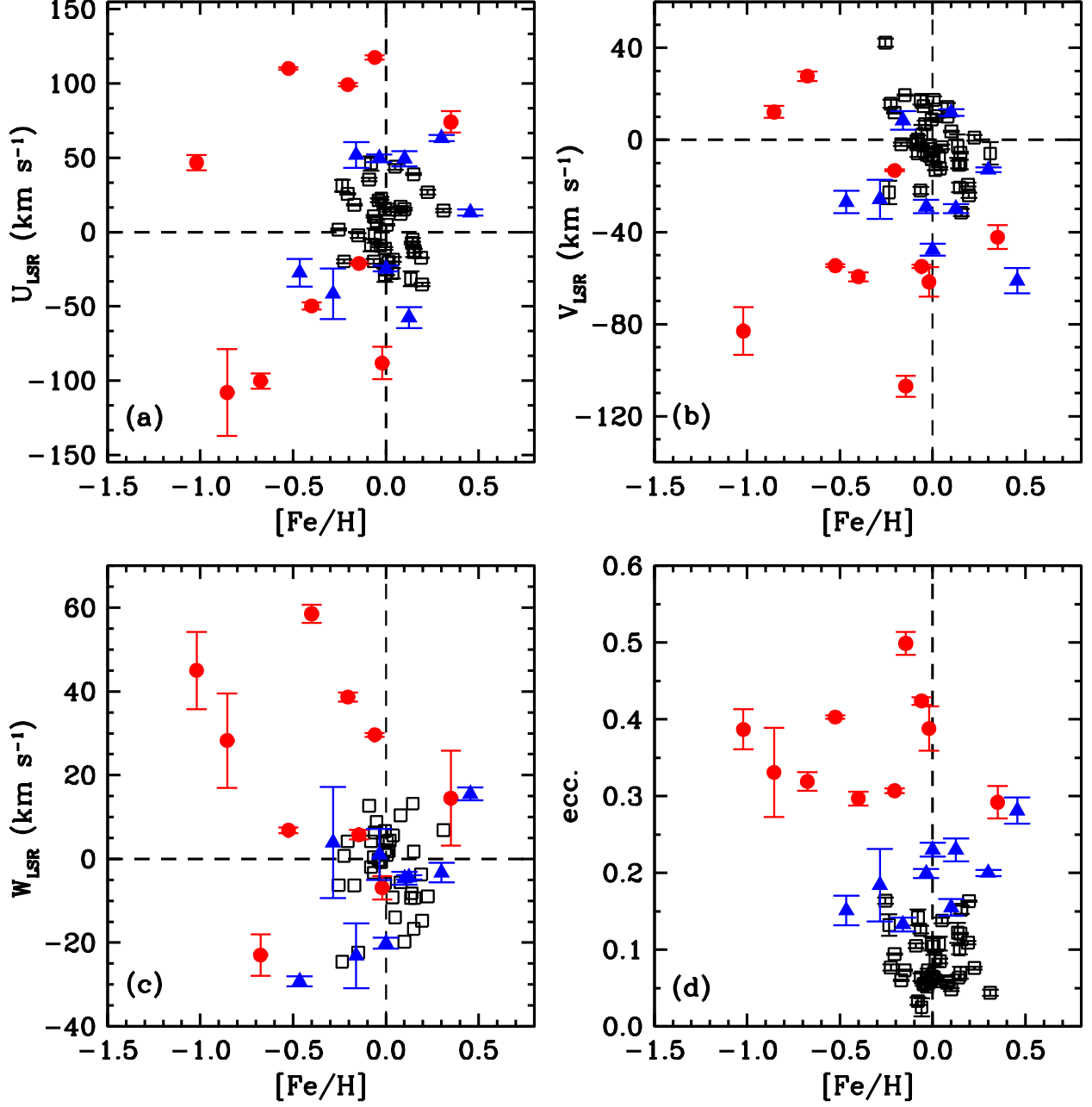


Fig. 15.— Correlations of kinematic components with $[\text{Fe}/\text{H}]$ metallicity: U_{LSR} in panel (a); V_{LSR} in panel (b); W_{LSR} in panel (c); and eccentricity in panel (d). The symbol colors are the same as those of Figure 13.

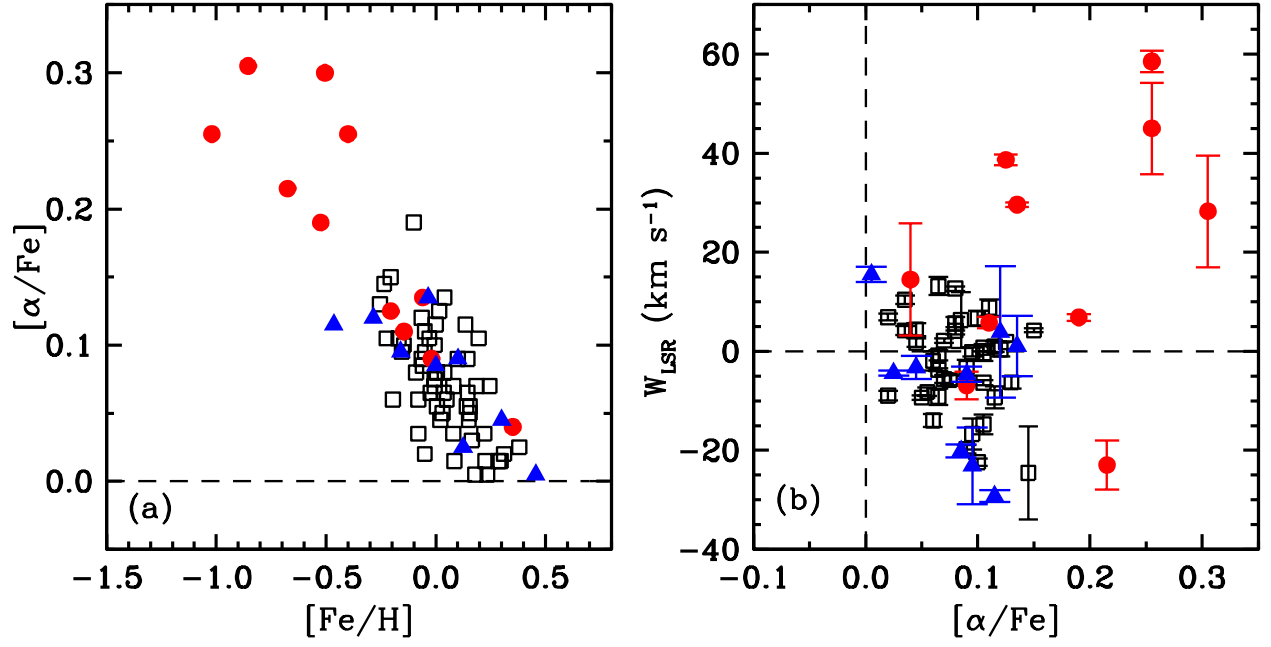


Fig. 16.— Panel (a): correlation of relative $[\alpha/\text{Fe}]$ abundance ratios with respect to metallicity $[\text{Fe}/\text{H}]$. Panel (b): comparison of vertical velocity component W_{LSR} with $[\alpha/\text{Fe}]$ values. The symbol colors are the same as those of Figure 13.

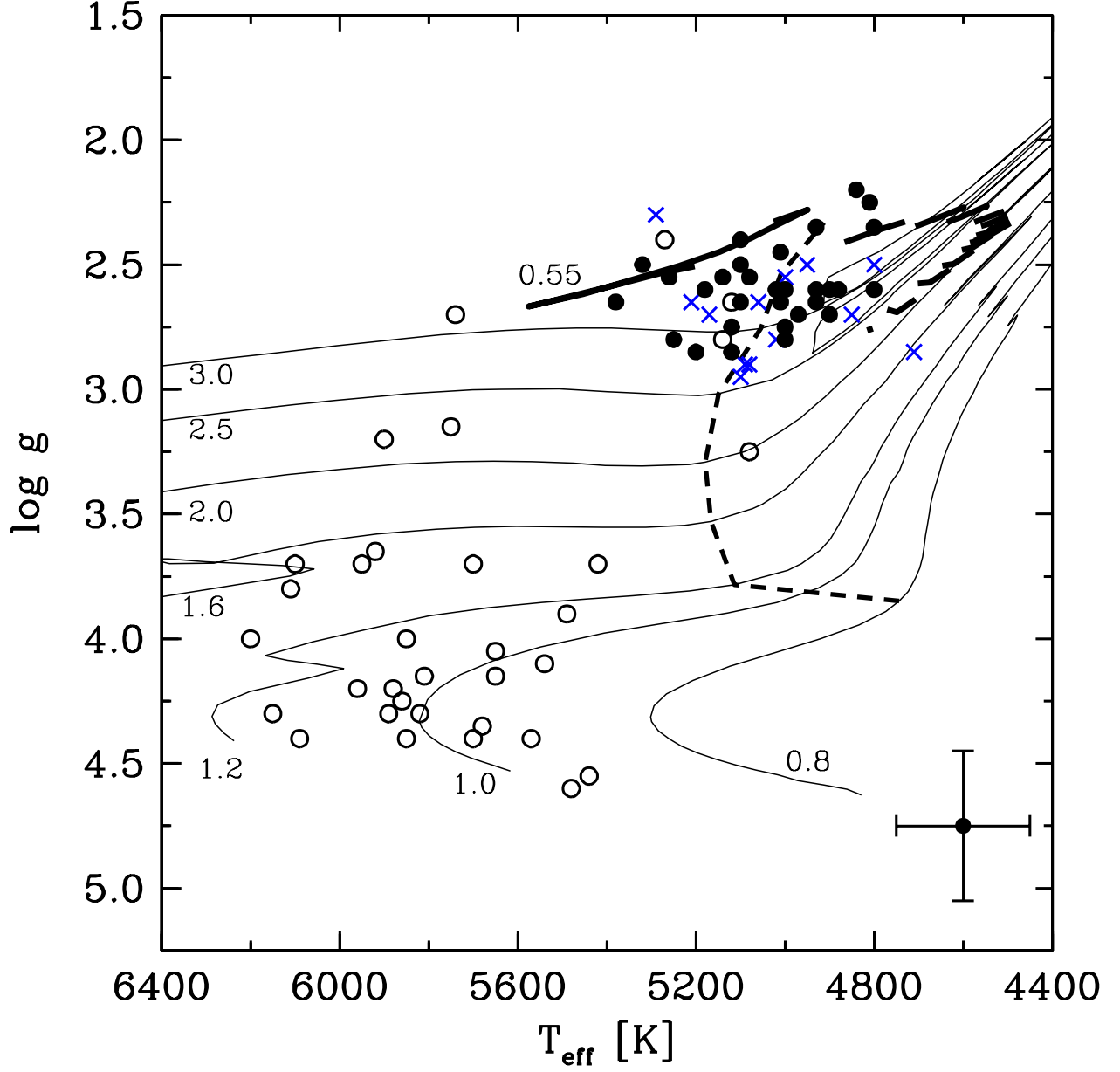


Fig. 17.— Evolutionary states of our program stars are shown on the spectroscopic $\log g$ - T_{eff} diagram. Stars with $^{12}\text{C}/^{13}\text{C} \leq 20$, $20 < ^{12}\text{C}/^{13}\text{C} \leq 30$ and $^{12}\text{C}/^{13}\text{C} > 30$ (no detection) are shown by filled circles, (blue) crosses and open circles, respectively.

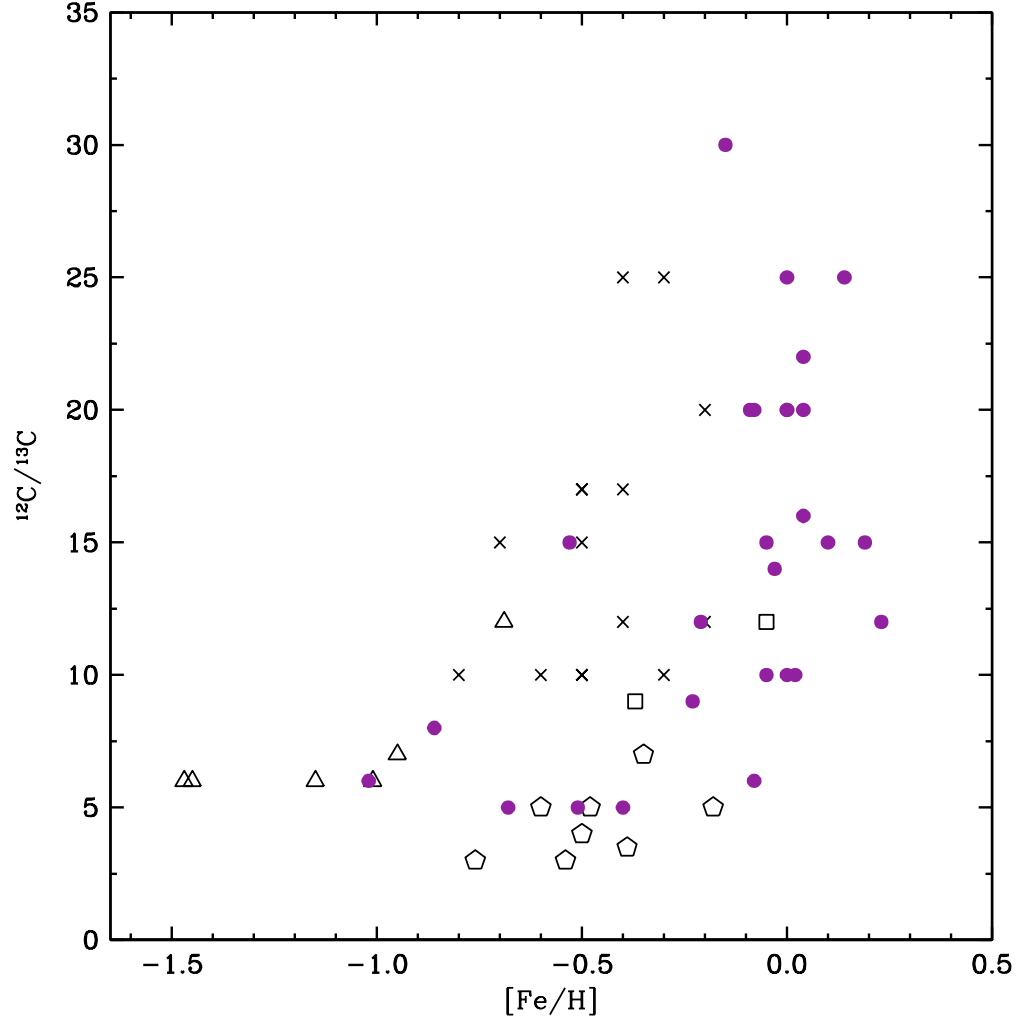


Fig. 18.— $^{12}\text{C}/^{13}\text{C}$ ratios (filled circles) as a function of the $[\text{Fe}/\text{H}]$ for RHB, RC and RC/RHB stars. Other RCs and RHBs from Lambert & Ries (1981) (open squares), Cottrell & Sneden (1986) (crosses), Gratton et al. (2000) (triangles) and Tautvaišienė et al. (2001) (open pentagons) are also plotted.

Table 1. Program Stars

Stars	B	V	K_s	$B-V$	$V-K_s$	π (mas)	σ_π (mas)	μ_α (mas/yr)	μ_δ (mas/yr)	RV
HIP 476	6.43	5.55	3.77	0.88	1.78	8.75	0.30	43.58	-5.96	...
HIP 3031	5.24	4.40	2.07	0.84	2.33	19.91	0.19	-229.04	-253.11	...
HIP 4197	7.56	6.71	4.51	0.85	2.20	4.78	1.16	-2.54	-46.24	...
HIP 4960	9.31	8.60	6.58	0.71	2.03	3.18	0.93	13.62	-20.59	...
HIP 5104	8.40	7.65	5.59	0.75	2.06	3.19	0.79	63.61	49.81	...
HIP 8404	6.88	5.91	3.86	0.97	2.05	10.16	0.47	-7.40	19.26	...
HIP 11924	8.63	8.00	6.50	0.63	1.50	11.02	0.77	-62.76	-57.96	...
HIP 13339	6.75	5.87	3.85	0.88	2.02	8.34	0.37	-25.49	-24.74	...
HIP 19611	7.60	6.60	4.44	1.00	2.17	6.87	0.77	-11.57	14.79	4.0
HIP 19740	5.71	4.89	2.97	0.82	1.92	9.83	0.64	-10.31	-30.01	...
HIP 27280	6.67	5.79	3.93	0.88	1.86	10.95	0.50	-32.08	-65.50	...
HIP 38801	9.14	8.48	6.83	0.66	1.65	1.64	1.35	-2.02	1.08	11.1
HIP 39326	6.91	6.30	4.82	0.61	1.48	8.71	0.40	6.87	-10.52	...
HIP 44154	6.13	5.23	3.15	0.90	2.08	11.03	0.28	-43.78	-35.03	...
HIP 45033	6.90	6.03	4.09	0.87	1.94	8.86	0.42	2.64	5.37	...
HIP 45158	6.68	5.73	3.54	0.95	2.19	10.73	0.37	-56.68	45.79	...
HIP 45412	6.80	5.99	3.86	0.81	2.13	7.69	0.54	-158.20	47.73	...
HIP 46325	9.13	8.38	6.76	0.74	1.63	11.28	1.00	13.88	-150.81	...
HIP 51179	7.49	6.65	4.53	0.84	2.12	8.05	0.56	-38.90	14.13	-25.2
HIP 51487	10.33	9.53	7.64	0.80	1.89	16.89	1.23	-6.09	-33.43	-14.5
HIP 54048	7.21	6.35	4.32	0.86	2.03	6.04	0.46	5.18	-5.06	-6.3
HIP 56194	7.47	6.55	4.41	0.93	2.14	5.66	0.41	-25.08	-25.49	...
HIP 57535	9.28	8.60	7.06	0.68	1.54	5.51	0.86	39.71	-7.07	...
HIP 57748	8.66	7.91	6.01	0.75	1.90	4.47	0.74	23.31	-19.18	-22.0
HIP 58269	9.41	8.70	7.18	0.71	1.51	10.32	1.12	80.71	-144.32	...
HIP 60140	8.50	7.67	5.60	0.83	2.07	3.75	0.79	-15.08	3.63	0.9
HIP 60485	5.64	4.77	2.82	0.87	1.96	8.44	0.24	12.64	11.43	...
HIP 60873	9.61	8.81	6.74	0.80	2.07	5.39	1.09	-58.88	2.83	-32.7
HIP 62325	6.66	5.70	3.44	0.96	2.26	22.15	0.35	279.34	-453.41	...
HIP 65900	8.93	8.34	7.00	0.59	1.34	16.74	0.91	-132.28	-29.61	...
HIP 66892	7.16	6.30	4.26	0.86	2.04	3.58	0.40	-85.88	13.24	...
HIP 70341	9.45	8.82	7.20	0.63	1.62	14.36	1.02	-147.37	-24.82	...
HIP 70344	7.80	7.22	5.79	0.58	1.43	14.20	0.78	20.49	-151.26	...
HIP 71837	6.50	5.56	3.41	0.94	2.15	8.09	0.33	-158.78	-112.62	...
HIP 72631	5.91	4.90	2.80	1.01	2.10	14.92	0.40	89.97	-124.57	...
HIP 75823	9.33	8.54	6.44	0.79	2.10	2.49	1.16	-23.31	9.96	...
HIP 78990	5.14	4.33	2.47	0.81	1.86	11.22	0.32	44.81	-45.42	...

Table 1—Continued

Stars	B	V	K_s	$B-V$	$V-K_s$	π (mas)	σ_π (mas)	μ_α (mas/yr)	μ_δ (mas/yr)	RV
HIP 80309	6.63	5.67	3.68	0.96	1.99	6.44	0.32	-29.31	34.26	...
HIP 80543	7.30	6.69	5.22	0.61	1.47	12.56	0.55	-0.46	-3.42	...
HIP 82014	9.67	8.92	7.14	0.75	1.78	8.23	0.80	-48.14	119.81	-19.9
HIP 85715	6.58	5.64	3.57	0.95	2.07	8.27	0.27	3.77	16.33	...
HIP 89008	6.49	5.57	3.65	0.92	1.92	8.28	0.30	12.72	11.12	...
HIP 89095	7.98	7.13	5.12	0.85	2.01	2.73	0.51	8.25	14.35	...
HIP 90906	8.33	7.44	5.29	0.89	2.15	3.39	0.73	4.63	14.69	...
HIP 91985	7.07	6.26	4.38	0.81	1.88	3.35	0.30	9.93	-2.23	...
HIP 92827	8.46	7.63	5.45	0.83	2.18	5.06	0.60	20.70	21.85	...
HIP 93940	8.79	8.25	6.88	0.54	1.37	7.81	0.83	37.43	7.16	-53.4
HIP 94598	6.91	6.04	4.05	0.87	1.99	4.79	0.42	3.33	-10.99	...
HIP 94779	4.73	3.80	1.76	0.93	2.04	26.27	0.10	60.07	122.83	...
HIP 98587	8.55	7.70	5.65	0.85	2.05	2.68	0.67	3.52	-26.95	...
HIP 100274	7.07	6.17	4.25	0.90	1.93	5.88	0.52	-3.10	6.71	...
HIP 103004	5.39	4.58	2.72	0.81	1.86	17.30	0.66	-75.44	-62.03	...
HIP 103734	6.99	6.01	4.04	0.98	1.97	5.21	0.33	-3.47	-6.42	...
HIP 113610	7.10	6.23	4.22	0.87	2.00	5.57	0.69	44.21	9.99	-14.7
HIP 114809	7.64	6.80	4.76	0.84	2.04	6.22	0.45	-0.29	12.71	...
HIP 115839	7.26	6.38	4.33	0.88	2.05	7.97	0.42	99.16	-21.66	...
HIP 118209	5.81	4.89	2.95	0.92	1.94	13.91	0.28	-57.13	-72.08	...
HD 9097	10.76	10.20	8.51	0.56	1.69
HD 84686	9.40	8.55	6.44	0.85	2.11
HD 96780	9.31	8.80	7.52	0.51	1.28
HD 101014	10.00	9.40	8.02	0.60	1.38
HD 141770	9.53	8.88	7.09	0.65	1.80
HD 166310	10.25	9.54	7.66	0.71	1.88
HD 221744	9.84	9.22	7.50	0.62	1.72
HD 235802	9.78	9.06	7.28	0.72	1.78
HD 242647	10.31	9.70	8.23	0.61	1.47
HD 243170	10.06	9.50	8.04	0.56	1.47
BD-14 1413	9.84	9.30	7.87	0.54	1.43
BD+27 2057	10.43	9.50	7.22	0.93	2.28
BD+31 2565	10.88	10.35	9.02	0.53	1.33
BD+32 2190	10.64	9.99	8.55	0.65	1.45
BD+41 2221	10.45	9.82	8.17	0.63	1.65
BD+45 1958	10.74	10.01	8.33	0.73	1.68
BD+45 2032	10.56	10.00	8.22	0.56	1.78

Table 1—Continued

Stars	B	V	K_s	$B-V$	$V-K_s$	π (mas)	σ_π (mas)	μ_α (mas/yr)	μ_δ (mas/yr)	RV
BD+54 2710	11.10	9.90	7.05	1.20	2.85
TYC 3720-324-1	11.30	10.50	8.54	0.80	1.96

Table 2. S/N ratios.

Stars	V	S/N		
		4500 Å	5500 Å	6500 Å
BD+27 2057	10.43	120	170	160
HD 84686	9.4	95	200	190
HIP 98587	8.55	115	250	210

Table 3. Model Atmosphere Parameters

Star	T_{eff} (K)	$\log g$	v_t (km s ⁻¹)	[Fe/H]
HIP 476	5140	2.80	1.35	-0.03
HIP 3031	5020	2.60	1.45	-0.53
HIP 4197	4800	2.50	1.00	-0.23
HIP 4960	5260	2.55	1.60	-1.02
HIP 5104	5100	2.50	1.55	-0.86
HIP 8404	4800	2.35	1.20	-0.05
HIP 11924	5850	4.00	1.00	0.30
HIP 13339	5120	2.85	0.95	0.23
HIP 19611	5080	2.90	1.25	0.00
HIP 19740	5100	2.40	1.20	-0.03
HIP 27280	5100	2.95	1.10	0.05
HIP 38801	5740	2.70	2.10	-0.06
HIP 39326	5750	3.15	1.60	-0.21
HIP 44154	5000	2.60	1.20	0.04
HIP 45033	5120	2.75	1.10	0.02
HIP 45158	4900	2.70	1.40	-0.23
HIP 45412	5080	2.55	1.55	-0.68
HIP 46325	5650	4.15	1.00	0.46
HIP 51179	5020	2.80	1.10	-0.15
HIP 51487	5440	4.55	1.30	-0.17
HIP 54048	5100	2.65	1.20	0.00
HIP 56194	4970	2.70	1.20	0.15
HIP 57535	5700	3.70	1.30	0.10
HIP 57748	5320	2.50	1.75	-0.08
HIP 58269	5820	4.30	1.10	0.35
HIP 60140	4930	2.65	0.85	-0.08
HIP 60485	5210	2.65	1.65	0.08
HIP 60873	5080	3.25	0.90	-0.47
HIP 62325	4710	2.85	0.90	-0.06
HIP 65900	6090	4.40	1.00	0.15
HIP 66892	5170	2.70	1.35	-0.02
HIP 70341	5700	4.40	0.90	0.00
HIP 70344	5950	3.70	1.25	-0.04
HIP 71837	4900	2.60	1.10	-0.15
HIP 72631	4800	2.60	1.20	-0.21
HIP 75823	5200	2.85	1.10	-0.29

Table 3—Continued

Star	T_{eff} (K)	$\log g$	v_t (km s ⁻¹)	[Fe/H]
HIP 78990	5380	2.65	1.55	0.10
HIP 80309	5000	2.75	1.50	-0.06
HIP 80543	5920	3.65	1.40	0.15
HIP 82014	5490	3.90	1.00	0.13
HIP 85715	4950	2.50	1.50	0.00
HIP 89008	5000	2.55	1.15	0.14
HIP 89095	5270	2.40	1.55	0.14
HIP 90906	4930	2.35	1.20	0.00
HIP 91985	5290	2.30	1.60	-0.06
HIP 92827	4850	2.70	0.85	0.04
HIP 93940	6110	3.80	1.30	0.20
HIP 94598	5010	2.45	1.30	-0.05
HIP 94779	4880	2.60	1.15	0.19
HIP 98587	4930	2.60	1.00	-0.16
HIP 100274	5010	2.65	1.15	0.08
HIP 103004	5250	2.80	1.35	-0.09
HIP 103734	5060	2.65	1.25	0.31
HIP 113610	5140	2.55	1.45	0.00
HIP 114809	5120	2.65	1.20	-0.26
HIP 115839	5000	2.80	1.30	-0.40
HIP 118209	5090	2.90	1.25	0.15
HD 9097	5540	4.10	0.80	0.18
HD 96780	6200	4.00	1.30	0.01
HD 84686	5180	2.60	1.75	-0.05
HD 101014	5880	4.20	0.80	0.30
HD 141770	5650	4.05	1.05	0.09
HD 166310	5480	4.60	1.35	0.17
HD 221744	5850	4.40	1.05	0.00
HD 235802	5680	4.35	1.25	0.25
HD 242647	5890	4.30	0.95	-0.20
HD 243170	6100	3.70	1.10	0.15
BD-14 1413	5900	3.20	1.60	-0.10
BD+27 2057	4810	2.25	1.25	-0.51
BD+31 2565	6150	4.30	1.15	0.03
BD+32 2190	5860	4.25	0.80	0.29
BD+41 2221	5810	4.15	1.15	0.22

Table 3—Continued

Star	T_{eff} (K)	$\log g$	v_t (km s ⁻¹)	[Fe/H]
BD+45 1958	5570	4.40	0.90	0.24
BD+45 2032	5420	3.70	0.80	-0.16
BD+54 2710	4840	2.20	1.45	0.04
TYC 3720-324-1	5960	4.20	1.05	0.38

Table 4. The adopted solar abundances.

Species	$\log\epsilon(X)$ (dex)	σ (dex)
Li I	1.02	
C I	8.53	0.06
C I (CH 4300)	8.38	
N I (CN 8000-8040)	8.2	
O I (7774)	8.91	0.01
O I (6300)	8.64	
Si I	7.55	0.14
Ca I	6.24	0.08
Fe I	7.5	0.08
Fe II	7.5	0.07
La II	1.17	
Eu II	0.52	

Table 5. $^{12}\text{C}/^{13}\text{C}$ ratios and their uncertainties

Stars	$^{12}\text{C}/^{13}\text{C}$	σ
HIP 45412	5	+2/-1.5
HIP 115839	5	+2/-1
BD+27 2057	5	+2/-1
HIP 57748	5	+2/-1
HIP 4960	6 ^a	...
HIP 5104	8	+2/-2
HIP 45158	9	+3/-1
HIP 45033	10	+2/-2
HIP 54048	10	+2/-1.5
HD 84686	10	+4/-2
HIP 72631	12	+3/-2
HIP 13339	12	+5/-2
HIP 19740	14	+4/-2
HIP 3031	15	+5/-5
HIP 71837	15	+3/-3
HIP 8404	15	+4/-2
HIP 78990	15	+3/-2
HIP 94779	15	+3/-2
HIP 44154	16	+3/-4
HIP 94598	17	+5/-3
HIP 98587	18	+5/-2
HIP 100274	20	+3/-4
HIP 75823	20	+8/-5
HIP 60140	20	+8/-4
HIP 103004	20	+8/-5
HIP 56194	20	+7/-5
HIP 90906	20	+5/-5
BD+54 2710	20	+5/-3
HIP 113610	20	+7/-4
HIP 80309	20	+5/-3
HIP 92827	22	+8/-4
HIP 4197	22	+4/-3
HIP 118209	22	+7/-3
HIP 60485	25	+5/-5
HIP 89008	25	+7/-5
HIP 85715	25	+5/-5
HIP 66892	30	>+10

Table 5—Continued

Stars	$^{12}\text{C}/^{13}\text{C}$	σ
HIP 62325	30	>+10
HIP 19611	30	>+10
HIP 91985	30	>+10
HIP 51179	30	>+10
HIP 103734	30	>+10
HIP 27280	30	>+10

Note. — ^a Taken from Gratton et al. (2000).

Table 6. Li abundances

Stars	T_{eff}	$\log g$	[Fe/H]	$\log \epsilon(\text{Li})$	$^{12}\text{C}/^{13}\text{C}$
HIP 45033	5120	2.75	0.02	0.93	10
HIP 94598	5010	2.45	-0.05	0.96	17
BD+54 2710	4840	2.20	0.04	0.56	20
HIP 92827	4850	2.70	0.04	0.74	22
HIP 4197	4800	2.50	-0.23	0.60	22
HIP 89008	5000	2.55	0.14	1.04	25
HIP 103734	5060	2.65	0.31	1.34	>30
HIP 19611	5080	2.90	0.00	1.56	>30
HIP 51179	5020	2.80	-0.15	0.75	>30
HIP 476	5140	2.80	-0.03	0.91	...
HIP 60873	5080	3.25	-0.47	0.81	...
BD+45 2032	5420	3.70	-0.16	1.54	...
HIP 82014	5490	3.90	0.13	2.04	...
HIP 80543	5920	3.65	0.15	3.26	...
HIP 11924	5850	4.00	0.30	1.70	...
HD 96780	6200	4.00	0.01	2.81	...
HD 141770	5650	4.05	0.09	2.26	...
BD+41 2221	5810	4.15	0.22	2.44	...
HIP 46325	5650	4.15	0.46	1.92	...
TYC 3720-324-1	5960	4.20	0.38	2.69	...
HD 101014	5880	4.20	0.30	2.20	...
BD+32 2190	5860	4.25	0.29	1.59	...
HIP 58269	5820	4.30	0.35	2.06	...
BD+31 2565	6150	4.30	0.03	2.57	...
HD 242647	5890	4.30	-0.20	2.09	...
HIP 65900	6090	4.40	0.15	2.72	...
HD 166310	5480	4.60	0.17	2.03	...

Table 7. Abundances

Stars	[Si I/Fe]	[Ca I/Fe]	[C I/Fe] _{CH}	[N I/Fe]	[O I/Fe]	[O I/Fe] _{NLTE}	[La/Fe]	[Eu/Fe]	¹² C/ ¹³ C	Evol.Phase
Thick Disk										
HIP 3031	0.21	0.18	-0.16	0.28	0.47	0.34	0.07	0.38	15	RHB
HIP 4960	0.27	0.24	-0.07	0.72	0.66	0.59	0.17	0.54	6	RHB
HIP 5104	0.31	0.31	-0.23	0.51	0.62	0.76	0.07	0.51	8	RHB
HIP 45412	0.22	0.22	-0.16	0.25	0.43	0.36	0.02	0.36	5	RHB
HIP 58269	0.12	-0.04	-0.01	0.39	0.07	0.00	-0.25	0.11	...	MS/SG
HIP 62325	0.17	0.10	-0.46	0.32	-0.04	0.10	-0.08	0.04	30	RGB
HIP 66892	0.10	0.08	-0.41	0.36	0.06	-0.13	0.25	0.12	30	—
HIP 71837	0.11	0.11	-0.42	0.44	0.15	0.21	0.02	0.21	15	RC/RHB
HIP 72631	0.18	0.08	-0.24	0.26	0.30	0.25	-0.01	0.25	12	RC
HIP 115839	0.27	0.24	-0.10	0.16	0.55	0.41	0.03	0.43	5	RHB
BD+27 2057	0.31	0.30	-0.32	0.07	0.35	0.45	-0.07	0.22	5	RHB/RC
Thin/Thick Disk										
HIP 11924	0.07	0.02	-0.06	0.18	0.12	0.10	-0.17	-0.18	...	MS/SG
HIP 46325	0.08	-0.07	-0.09	0.15	0.04	-0.08	0.06	-0.19	...	MS/SG
HIP 57535	0.12	0.06	-0.17	0.05	0.19	0.04	-0.10	-0.01	...	SG
HIP 60873	0.09	0.14	-0.13	0.20	0.26	0.19	0.22	0.38	...	RGB
HIP 70341	0.10	0.07	0.00	0.10	...	0.21	0.04	0.24	...	MS/SG
HIP 70344	0.13	0.15	-0.16	0.15	...	0.23	0.05	0.11	...	SG
HIP 75823	0.09	0.16	-0.30	0.43	0.06	0.01	0.08	0.09	20	RHB
HIP 82014	0.03	0.02	-0.10	0.11	0.13	0.00	-0.10	0.04	...	SG
HIP 98587	0.08	0.11	-0.66	0.66	-0.16	0.04	0.10	0.08	18	RC/eAGB
Thin Disk										
HIP 476	0.08	0.13	-0.25	0.33	0.04	...	0.18	0.02	...	RGB
HIP 4197	0.19	0.09	-0.68	0.48	0.01	0.17	0.04	0.06	22	RC/RGB
HIP 8404	0.11	0.11	-0.45	0.05	-0.16	-0.22	0.06	-0.07	15	RC
HIP 13339	-0.04	0.08	-0.39	0.03	-0.23	-0.30	0.13	-0.04	12	RHB
HIP 19611	0.04	0.12	-0.31	0.03	-0.13	-0.05	0.14	0.05	30	RGB/RHB

Table 7—Continued

Stars	[Si I/Fe]	[Ca I/Fe]	[C I/Fe] _{CH}	[N I/Fe]	[O I/Fe]	[O I/Fe] _{NLTE}	[La/Fe]	[Eu/Fe]	¹² C/ ¹³ C	Evol.Phase
HIP 19740	0.02	0.12	-0.47	0.41	-0.17	-0.28	0.16	-0.01	14	RHB
HIP 27280	0.02	0.10	-0.38	0.26	-0.12	-0.14	0.15	0.00	30	RGB/RHB
HIP 38801	0.04	0.13	-0.37	0.63	0.11	0.22	0.29	0.24	...	HB
HIP 39326	0.10	0.21	-0.18	0.43	0.23	0.36	0.01	0.09	...	SG
HIP 44154	0.08	0.08	-0.45	0.19	-0.20	-0.20	0.14	0.04	16	RHB
HIP 45033	-0.01	0.10	-0.44	0.33	-0.18	-0.14	0.13	-0.01	10	RHB
HIP 45158	0.14	0.07	-0.35	0.36	0.16	0.09	0.26	0.25	9	RC
HIP 51179	0.09	0.11	-0.47	0.46	-0.08	0.05	0.13	0.00	30	RHB
HIP 51487	0.06	0.15	-0.04	0.14	...	0.23	0.29	-0.06	...	MS
HIP 54048	0.04	0.11	-0.59	0.37	-0.11	-0.19	0.15	0.05	10	RHB
HIP 56194	0.10	0.04	-0.48	0.35	-0.12	-0.15	0.06	0.01	20	RC/RGB
HIP 57748	0.10	0.02	-0.20	0.09	0.02	0.11	-0.30	-0.11	6	RHB
HIP 60140	0.05	0.02	-0.49	0.18	-0.25	-0.10	0.16	0.11	20	RHB/RC
HIP 60485	0.06	0.08	-0.47	0.52	-0.08	-0.06	0.20	0.00	25	—
HIP 65900	0.03	0.08	-0.03	0.01	0.07	0.19	...	MS
HIP 78990	0.02	0.16	-0.42	0.50	-0.03	-0.24	0.16	-0.06	15	RHB
HIP 80309	0.14	0.11	-0.33	0.47	-0.03	-0.12	0.03	0.08	20	RGB
HIP 80543	0.10	0.09	0.01	0.04	...	0.09	-0.05	-0.07	...	SG
HIP 85715	0.12	0.03	-0.42	0.41	-0.03	-0.05	0.08	-0.06	25	RC/RHB
HIP 89008	0.05	0.06	-0.36	0.04	-0.31	-0.28	0.00	-0.17	25	RGB/RHB
HIP 89095	0.10	0.14	-0.40	0.40	-0.19	-0.15	-0.11	-0.06	...	HB?
HIP 90906	0.14	0.09	-0.59	0.51	-0.21	-0.06	-0.10	-0.12	20	RC/RHB
HIP 91985	0.05	0.12	-0.41	0.62	-0.19	-0.15	0.06	-0.01	30	HB?
HIP 92827	0.13	0.00	-0.75	0.72	-0.24	-0.10	-0.12	-0.09	22	RC
HIP 93940	0.12	0.09	-0.10	...	-0.02	0.11	-0.14	0.07	...	SG
HIP 94598	0.10	0.09	-0.63	0.49	-0.13	-0.15	0.11	0.00	17	RHB/eAGB
HIP 94779	0.09	0.04	-0.53	0.14	-0.28	-0.15	-0.10	-0.06	15	RC/RHB
HIP 100274	0.02	0.05	-0.42	0.24	-0.05	-0.09	0.06	0.02	20	RC/RGB

Table 7—Continued

Stars	[Si I/Fe]	[Ca I/Fe]	[C I/Fe] _{CH}	[N I/Fe]	[O I/Fe]	[O I/Fe] _{NLTE}	[La/Fe]	[Eu/Fe]	¹² C/ ¹³ C	Evol.Phase
HIP 103004	0.06	0.10	-0.26	0.50	-0.10	0.11	0.12	0.13	20	RHB
HIP 103734	0.05	-0.01	-0.34	0.28	-0.16	-0.23	-0.06	-0.12	30	RGB
HIP 113610	0.08	0.13	-0.56	0.45	-0.08	-0.16	0.13	0.02	20	RHB
HIP 114809	0.13	0.14	-0.27	0.32	0.11	0.16	0.05	0.11	...	RHB
HIP 118209	0.03	0.06	-0.42	0.25	-0.15	-0.29	0.17	0.08	22	RGB/RHB
HD 9097	0.05	-0.04	-0.06	0.11	...	0.17	0.01	0.25	...	MS/SG
HD 84686	0.13	-0.09	-0.10	0.15	0.14	0.05	-0.26	0.24	10	RHB
HD 96780	0.12	0.14	-0.04	...	0.18	0.15	0.04	0.08	...	MS/SG
HD 101014	0.04	-0.02	-0.13	0.20	...	0.04	0.00	-0.06	...	MS/SG
HD 141770	0.03	0.00	-0.04	0.20	0.03	0.15	0.03	0.06	...	MS/SG
HD 166310	0.04	0.02	-0.39	0.14	...	0.15	0.02	0.24	...	MS
HD 221744	-0.01	0.13	-0.15	0.35	0.14	0.04	0.12	0.14	...	MS
HD 235802	0.12	0.02	-0.26	0.22	...	0.20	...	-0.17	...	MS
HD 242647	0.02	0.11	-0.17	0.11	...	0.33	0.17	0.20	...	MS
HD 243170	0.03	0.09	-0.20	0.03	...	-0.03	...	SG
BD-14 1413	0.19	0.19	-0.17	0.35	0.00	0.14	...	SG
BD+31 2565	0.07	0.03	-0.08	0.10	0.25	0.04	...	MS
BD+32 2190	0.03	0.00	-0.01	0.23	...	0.05	-0.13	0.07	...	MS/SG
BD+41 2221	0.05	0.02	0.04	0.19	0.13	0.04	-0.05	0.06	...	MS/SG
BD+45 1958	0.02	-0.02	-0.24	0.29	...	0.04	-0.14	0.02	...	MS
BD+45 2032	0.08	0.12	-0.29	0.14	-0.02	0.20	0.14	0.38	...	SG
BD+54 2710	0.16	0.11	-0.60	0.52	-0.22	-0.05	0.10	-0.01	20	RC
TYC 3720-324-1	0.10	-0.05	-0.05	0.16	...	0.04	0.07	-0.29	...	MS/SG

Note. — Due to lack of parallax information we were unable to investigate the kinematical parameters of BD+27 2057 but by taking into previous studies, e.g. Stetson & Aikman (1987), Uggren (1962, 1963) and Tautvaišienė et al. (2001), we list it as a thick disk member in the table.

Table 8. Kinematics

Stars	U_{LSR} (km s ⁻¹)	$\sigma_{U_{\text{LSR}}}$ (km s ⁻¹)	V_{LSR} (km s ⁻¹)	$\sigma_{V_{\text{LSR}}}$ (km s ⁻¹)	W_{LSR} (km s ⁻¹)	$\sigma_{W_{\text{LSR}}}$ (km s ⁻¹)	Membership
HIP 62325	117.5	1.6	-55.0	0.7	29.6	0.5	Tk
HIP 3031	110.1	0.7	-54.6	0.7	6.9	0.7	Tk
HIP 5104	-108.0	29.2	12.1	2.6	28.3	11.3	Tk
HIP 71837	-21.1	1.0	-106.9	4.5	5.8	1.1	Tk
HIP 66892	-88.2	11.0	-61.7	6.5	-6.9	2.8	Tk
HIP 72631	99.2	1.1	-13.2	0.4	38.7	1.1	Tk
HIP 45412	-100.2	5.2	27.7	2.0	-22.9	5.0	Tk
HIP 4960	46.7	5.2	-83.0	10.4	45.0	9.2	Tk
HIP 115839	-49.8	2.5	-59.4	2.0	58.5	2.2	Tk
HIP 58269	74.1	7.2	-42.2	5.2	14.5	11.3	Tk
HIP 82014	-57.6	7.0	-29.8	2.0	-4.4	0.5	Tk/Tn
HIP 11924	63.3	2.1	-13.0	1.1	-3.2	2.3	Tk/Tn
HIP 46325	13.2	2.1	-61.1	5.4	15.5	1.5	Tk/Tn
HIP 70344	49.6	2.4	-29.0	2.9	1.0	6.1	Tk/Tn
HIP 98587	51.8	8.6	8.4	4.0	-23.1	7.8	Tk/Tn
HIP 70341	-24.7	1.9	-47.7	2.7	-20.1	1.3	Tk/Tn
HIP 57535	49.4	5.1	11.9	1.4	-4.6	1.5	Tk/Tn
HIP 75823	-41.6	17.0	-25.8	8.5	3.9	13.2	Tk/Tn
HIP 60873	-27.4	9.3	-26.9	4.9	-29.3	1.2	Tk/Tn
HIP 57748	46.1	4.8	-5.9	1.4	-1.9	1.9	Tn
HIP 27280	43.9	1.9	-3.0	1.0	-14.0	1.3	Tn
HIP 4197	31.2	4.0	-22.8	5.1	-24.6	9.4	Tn
HIP 93940	-35.2	1.2	-24.1	1.2	-14.7	2.0	Tn
HIP 114809	1.7	0.6	42.2	1.7	-6.3	1.2	Tn
HIP 118209	38.9	0.7	-5.5	0.5	1.7	0.8	Tn
HIP 103004	35.4	1.2	-1.4	1.9	12.7	0.5	Tn
HIP 65900	-12.6	1.3	-31.6	1.6	-9.4	0.5	Tn
HIP 89095	-31.4	5.0	-2.7	5.1	-9.3	2.2	Tn
HIP 113610	-29.0	4.6	-8.3	0.9	6.7	1.6	Tn
HIP 92827	-27.7	3.6	-7.2	4.6	-9.2	1.7	Tn
HIP 51179	-2.3	1.6	19.5	0.4	-22.4	0.7	Tn
HIP 80309	-19.7	1.6	-22.0	1.6	0.4	1.4	Tn
HIP 39326	25.7	0.4	11.9	0.4	4.2	0.4	Tn
HIP 13339	26.8	1.6	1.0	1.2	-9.0	1.0	Tn
HIP 94779	-17.2	0.2	-19.4	0.9	-3.7	0.3	Tn
HIP 90906	-25.0	4.0	-6.4	3.1	0.9	1.1	Tn

Table 8—Continued

Stars	U_{LSR} (km s ⁻¹)	$\sigma_{U_{\text{LSR}}}$ (km s ⁻¹)	V_{LSR} (km s ⁻¹)	$\sigma_{V_{\text{LSR}}}$ (km s ⁻¹)	W_{LSR} (km s ⁻¹)	$\sigma_{W_{\text{LSR}}}$ (km s ⁻¹)	Membership
HIP 78990	15.5	0.9	3.7	0.3	-19.7	0.8	Tn
HIP 45158	-19.7	1.3	15.8	1.8	0.7	0.7	Tn
HIP 56194	-5.2	1.3	-20.6	2.1	13.2	1.8	Tn
HD 96780	-20.1	...	-13.1	...	1.9	...	Tn
HIP 80543	-13.4	3.3	-10.7	2.1	-16.7	3.2	Tn
HIP 44154	-18.5	1.5	-12.4	0.5	5.6	1.4	Tn
HIP 19740	22.5	1.0	-2.3	0.8	-0.8	1.1	Tn
HIP 94598	21.3	1.4	6.8	1.7	-0.1	0.9	Tn
HIP 100274	12.2	1.2	14.3	1.7	10.5	0.8	Tn
HIP 60485	17.1	0.4	10.2	0.4	-5.6	0.8	Tn
HIP 91985	10.6	0.7	17.4	1.9	-3.3	1.6	Tn
HIP 51487	18.3	0.4	-1.8	0.7	-6.3	0.5	Tn
HIP 45033	15.2	1.4	10.3	0.7	4.4	1.3	Tn
HIP 8404	7.3	1.0	14.7	0.8	8.8	1.7	Tn
HIP 19611	4.8	0.5	17.4	1.6	4.2	0.7	Tn
HIP 54048	15.9	0.7	8.8	0.4	2.2	0.4	Tn
HIP 103734	14.5	1.0	-5.9	4.9	6.9	0.7	Tn
HIP 89008	-7.3	0.9	-10.7	1.7	-8.2	0.9	Tn
HIP 85715	-11.1	1.1	-8.1	1.4	-5.8	1.0	Tn
HIP 476	-9.4	0.8	-6.4	1.4	-0.4	1.5	Tn
HIP 60140	-8.7	4.1	0.2	1.7	4.2	0.9	Tn
HIP 38801	-2.5	4.8	2.1	4.5	6.3	5.6	Tn